# Coordination of escape and spatial navigation circuits orchestrate versatile flight from threats

**Weisheng Wang**[#,1], **Peter J. Schuette**[#,1], **Jun Nagai**[2], **Brooke Christine Tobias**[1], **Fernando Midea Cuccovia V. Reis**[1], **Shiyu Ji**[1], **Miguel A. X. de Lima**[3], **Mimi Q. La-Vu**[1], **Sandra Maesta-Pereira**[1], **Meghmik Chakerian**[1], **Saskia J. Leonard**[1], **Lilly Lin**[1], **Amie L. Severino**[2], **Catherine M. Cahill**[4], **Newton S. Canteras**[3], **Baljit S. Khakh**[2], **Jonathan C. Kao**[5], **Avishek Adhikari**[1,7,*]

[1]Department of Psychology, University of California, Los Angeles, Los Angeles, CA, 90095, USA

[2]Department of Physiology, University of California, Los Angeles, Los Angeles, CA, 90095, USA

[3]Department of Anatomy, Institute of Biomedical Sciences, University of Sao Paulo, Sao Paulo, SP, 05508-000, Brazil

[4]Department of Psychiatry and Biobehavioral Sciences, University of California, Los Angeles, Los Angeles, CA, 90095, USA

[5]Department of Electrical and Computer Engineering, University of California, Los Angeles, Los Angeles, CA, 90095, USA

[7]Lead Contact

[#] These authors contributed equally to this work.

## SUMMARY

Naturalistic escape requires versatile context-specific flight with rapid evaluation of local geometry to identify and use efficient escape routes. It is unknown how spatial navigation and escape circuits are recruited to produce context-specific flight. Using mice, we show activity in cholecystokinin-expressing hypothalamic dorsal premammillary cells (PMd-cck) is sufficient and necessary for context-specific escape that adapts to each environment's layout. Contrastingly, numerous other nuclei implicated in flight only induced stereotyped panic-related escape. We reasoned the PMd can induce context-specific escape because it projects to both escape and spatial navigation nuclei. Indeed, activity in PMd-cck projections to thalamic spatial navigation circuits

[*]Correspondence: avi@psych.ucla.edu.

are only necessary for context-specific escape induced by moderate threats, but not panic-related stereotyped escape caused by perceived asphyxiation. Conversely, the PMd projection to the escape-inducing dorsal periaqueductal gray projection is necessary for all escapes tested. Thus, PMd-cck controls versatile flight, engaging spatial navigation and escape circuits.

## eTOC Blurb

-Wang et al., show that the hypothalamic dorsal premammillary nucleus (PMd), but not other hypothalamic nuclei, controls both versatile escape from threats as well as panic-related simple flight in mice. The PMd engages spatial-navigation outputs in the thalamus only during context-specific versatile escape. In contrast, the PMd recruits brainstem outputs during both context-specific and panic-related flight.

## Graphical Abstract
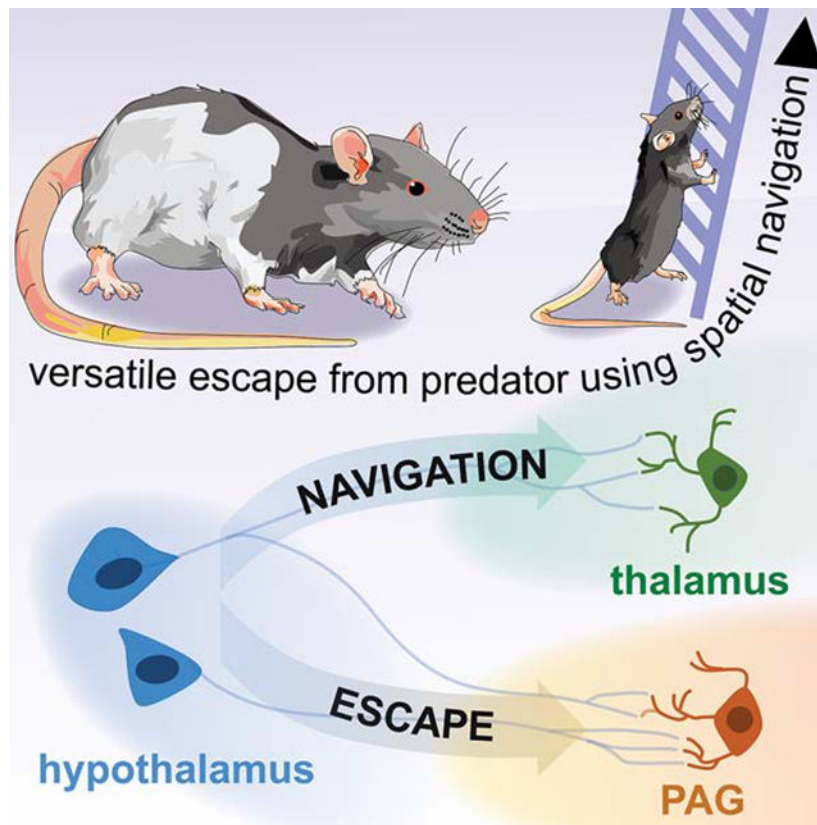


## INTRODUCTION

Animals rapidly escape from imminent threats (Perusini and Fanselow, 2015). Escape frequently occurs in complex contexts, in which animals quickly assess the local layout to find efficient flight paths (Blank, 2018; Hedenström and Rosén, 2001; Heithaus et al., 2009; Woodbury, 1986). These escapes require context-specific plans and precise coordination of spatial navigation and flight to identify and use effective escape routes. For example, escaping a burning building requires rapid evaluation of the floor's architecture to locate and

use the most direct route to safety (Kobes et al., 2010). Stereotyped actions such as aimless jumping and running do not allow escape in such situations. However, the majority of escape studies use simple environments (Chou et al., 2018; Lecca et al., 2017; Li et al., 2018; Shang et al., 2018; Xiong et al., 2015). In these assays, stereotyped actions such as running in any direction away from threat is often sufficient to reach safety. For instance, mice escaping a loud sound (Xiong et al., 2015) or a looming stimulus (Shang et al., 2018) in an empty box only have to run away from these stimuli in any direction. Contrary to escapes that require context-specific plans, flight in simple environments such as an empty box does not require sophisticated spatial navigation skills or any knowledge of the environment's layout. As escape is generally studied in simple environments, it is unknown how spatial navigation is integrated with escape to produce context-specific escape requiring flexible decision-making to identify efficient flight routes in complex environments.

The region most strongly implicated with escape is the brainstem dorsolateral gray (dlPAG) (Deng et al., 2016; Evans et al., 2018). DLPAG activation causes flight, (Deng et al., 2016), and dlPAG inhibition profoundly impairs threat-induced escape (Aguiar and Guimarães, 2009). Excitatory inputs to the dlPAG, such as the superior colliculus also are critical for vital and rapid stimulus-driven escape (Evans et al., 2018; Kragel et al., 2019), but this behavior does not require complex spatial navigation skills which are often necessary in flight occuring in naturalistic settings. Hypothalamic PAG inputs, such as the ventromedial and dorsomedial hypothalamus, also control flight (Johnson and Shekhar, 2012; Johnson et al., 2008; Wang et al., 2015). However, the strongest hypothalamic projection to the dlPAG has not been investigated.

The largest hypothalamic input to glutamatergic flight-inducing dlPAG cells is the dorsal premammillary nucleus (PMd) (Tovote et al., 2016). PMd lesions impair predator-induced defense, and this region is strongly activated by escape-inducing threats (Cezario et al., 2008). The PMd's most remarkable feature is its unique connectivity, as it interfaces between spatial navigation and defensive circuits. Its two main outputs are the escape-inducing dlPAG and a navigation and memory -related structure named the anteromedial ventral thalamic nucleus (amv) (Canteras and Swanson, 1992). Amv lesions impair spatial navigation and contextual memory (Jankowski et al., 2013). The amv also has cells that encode head direction (Bassett et al., 2007) and projects to canonical navigation regions such as the entorhinal cortex and the subiculum (Jankowski et al., 2013). Considering the role of the PMd in defense, and its connectivity with defense and spatial navigation networks, we hypothesized the PMd orchestrates the coordination of contextual navigation and flight necessary for strategic context-specific escape.

Here, we directly studied the role of cholecystokinin (cck)- expressing PMd cells in escape. We show PMd-cck cell activity is sufficient and necessary for both context-specific and stereotyped escape. In contrast, other hypothalamic nuclei only affected stereotyped defensive behaviors but not context-specific flight. Interestingly, PMd-cck cells recruit the amv only in tasks that require context-specific escape. In contrast, the PMd-cck projection to the dlPAG is necessary for both context-specific and stereotyped escapes. Thus, the PMd is the first identified region that produces versatile context-specific flight by coordinated recruitment of escape and spatial navigation networks.

# RESULTS

## PMd controls context-specific escape.

*In situ* hybridizations show most PMd neurons expressed VGLUT2 (87%) and cholecystokinin (cck) (Figure S1A–D). GABAergic markers were not expressed in the PMd (S1E-M). We used a cck-cre line to specifically target the PMd, as cck expression is more restricted to the PMd compared to VGLUT2. To bidirectionally control the activity of PMd-cck cells, we show that the ligand clozapine-n-oxide (CNO) respectively depolarized or hyperpolarized PMd-cck cells expressing hM3Dq or hM4Di (Figure 1A–B).

We next investigated if PMd activity modulates versatile context-specific escape induced by threats. We expressed DREADDs in PMd-cck cells (Figure 1C) and exposed mice to novel escape-inducing assays according to a planned timeline (Figure 1D). In the rat assay (Figure 1E), mice were placed in either the presence of an awake rat or a toy rat. To escape from the rat, mice found a ladder located in a corner and climbed it to access a safe burrow. After resting in the burrow for one-minute, mice were gently pushed to descend the ladder (Figure 1E and Video S1). The number of escape climbs in 20 minutes were counted (the 20 minutes include the 1-min rest periods). We opted for climbing escape routes because, in order to escape, mice could only climb one specific location, requiring spatial navigation and a tridimensional understanding of the context. Mice are also less likely to use climbing routes by chance due to hyper locomotion or other strategies without context-specific escape. Mice expressing hM3Dq, hM4Di or mcherry in PMd-cck cells were exposed twice to the rat and the toy rat after being treated with CNO or saline in separate days. Chemogenetic inhibition and excitation of PMd-cck cells respectively decreased and increased the number of climbs away from the live rat (Figure 1F–G). These manipulations did not change behavior in the safe toy rat assay, indicating that PMd-cck cells are selectively controlling escape from threats, rather than generally increasing exploration (Figure 1F–G, see also detailed statistical information for all Figures in Table S1).

We next investigated how the PMd controlled escape induced by threats of different intensities in the same context. We developed two assays: exposure to a heated floor and $CO_2$. In the heated floor assay, mice climbed a cylinder wrapped in thin mesh to avoid a heated floor (43°C) or an unheated control floor at room temperature (Figure 1H, left). Mice climbed down on their own. The number of climbs in 20 minutes was counted.

To measure panic-related stereotyped escape, (Blanchard et al., 2001; Johnson et al., 2011) we counted the number of jumps in mice exposed to 15% $CO_2$ or air for 10 minutes (Figure 1H, right). Identical chambers containing the climbing escape route were used in the $CO_2$ and heated floor assays. We elicited panic with $CO_2$ rather than a higher heated temperature to avoid skin burns.

Mice mostly climbed in the rat and heated floor assays and jumped in the $CO_2$ test (Figure 1I). In the heated floor and rat assays, escaping from threats required knowledge of the contextual layout. Thus, climbing in the rat and heated floor assays was used as a measure of context-specific flight that requires spatial navigation in three dimensions. In contrast, jumping in the $CO_2$ assay did not use context-specific escape, as mice aimlessly jumped

from anywhere. The interval between climbing escapes in rat and heated floor assays was higher than between jumps in $CO_2$, in agreement with the view that panic jumping may be a more reflexive escape than climbing. In both assays, climbing provided longer relief from the threat, as mice could decrease threat exposure for as long as they clung on the climbing route and remained far from the heated floor or from the highest $CO_2$ concentration at the bottom (Figure 1J). Indeed, in the $CO_2$ assay, climbs provided longer-lasting avoidance of threat than jumps (Figure 1K). Though climbing provided more effective threat avoidance, exposure to the panicogenic agent $CO_2$ shifted behavior from context-specific climbs in the heated floor assay to panic-related jumps in the $CO_2$ assay (Figure 1I).

Chemogenetic inhibition and excitation of PMd-cck cells respectively decreased and increased escape attempts in both heated floor and $CO_2$ assays (Figure 1L–O, see also detailed time course in Figure S2A). Thus, PMd-cck activity is necessary and sufficient to control versatile context-specific flight and panic-related stereotyped escapes, which are caused respectively by moderate and high intensity threats. These results could not be attributed to changes in pain perception, anxiety or overall locomotion (Figure S2B–D). Compared to the rat, the toy rat elicited fewer escapes and less avoidance, demonstrating that the toy rat is an appropriate safe control stimulus Figure S3A–B).

We next investigated if context-specific escape is specific to the PMd or if it is also present in other hypothalamic nuclei involved in escape. Thus, we chemogenetically excited the dorsomedial hypothalamus, a nucleus that mediates panic-related escape (Johnson and Shekhar, 2012; Johnson et al., 2008). This manipulation did not change context-specific climbs (Figure S3C). However, dorsomedial hypothalamic excitation increased panic-related stereotyped jumping in the $CO_2$ assay (Figure S3C), indicating it only controls stereotyped flight. We then activated the dorsomedial portion of the ventromedial hypothalamus (VMHdm). This nucleus is highly interconnected with the PMd (Canteras and Swanson, 1992; Comoli et al., 2000) and activation of SF1-expressing VMHdm cells induces freezing and flight (Wang et al., 2015). Excitation of VMH-SF1 cells did not alter escape in any assay (Figure S3D). However, exciting these cells, but not the PMd-cck or dorsomedial hypothalamus-syn cells, increased freezing in the rat assay (Figure S3H), in agreement with the role of the VMHdm in predator-induced defense (Martinez et al., 2008; Silva et al., 2016). Thus, excitation of the DMH and the VMHdm did not induce context-specific escapes.

### Dorsal premammillary nucleus (PMd) activation induced context-specific escape,

We next investigated the effects of optogenetic activation of PMd-cck cells in contexts requiring distinct strategies to escape (Figure 2B). Optogenetic activation of PMd-cck cells (20 Hz, Figure 2A and Figure S4A–C) in an empty box elicited running and jumping (Figure 2C upper panel, Figure S4D–E and Video S2), but not freezing, even at lower stimulation intensities (Figure S4E). When mice were placed in the same box in the presence of a rope or a series of blocks that could be climbed to allow escape (Figure 2B), PMd-cck stimulation did not cause jumping. Instead, it caused escape through the newly provided escape routes. All PMd-cck ChR2 mice escaped using these diverse new routes within 30 seconds of optogenetic stimulation without any prior training (Figure 2C, 2nd and 3rd panels). Thus,

PMd-cck stimulation created context-specific flight, even in unfamiliar and complex environments. In contrast, activation of ChR2-expressing VMHdm SF1 cells increased escape jumps, but did not consistently produce escape from the complex upwards step box (Figure S3E–G).

To identify other regions that may control context-specific escape, we optogenetically activated numerous hypothalamic and brainstem nuclei that showed threat-induced increases in fos expression (Figure S5A–B). Activation of several nuclei induced jumping and freezing (Figure S5D and S5H–K). Remarkably, among 7 tested nuclei, only PMd optogenetic activation induced escape from the upwards step box (Figure S5F, and video S3), even though animals had no prior exposure to this box (Figure S5E). In contrast, dlPAG activation did not induce escape from the complex upwards step box with low or high light power optogenetic stimulation (Figure S5G). In a box with two context-specific escape routes PMd stimulation induced actions that quickly adapted to allow escape, even if the number and type of escape routes were changed (Video S4, $n$=4). Thus, PMd stimulation flexibly induced escape in rapidly changing environments.

**PMd activation induced aversion and autonomic activation**

To study if PMd-cck stimulation is aversive, we tested whether PMd-cck ChR2 mice nose-poked to stop optogenetic stimulation. Mice received optogenetic stimulation until they nose-poked. This halted stimulation for 5 seconds, after which stimulation resumed until another nose poke occured. Data was collected for 10 minutes following 2 minutes of habituation and without any pre-training. Blue light power in the nose poke test was lower than that used in escape assays (Figure 2C) to avoid overt escape (see Methods). Mice expressing ChR2-YFP, but not YFP, in PMd-cck cells learned to nose-poke to avoid PMd-cck stimulation (Figure 2D). Importantly, PMd-cck ChR2 mice did not nose poke more than YFP mice in an inactive nose poke that did not halt optogenetic stimulation (Figure S4G). PMd-cck stimulation also caused avoidance in a real-time place preference task (Figure 2E–F). This avoidance persisted for 10 minutes following the end of the stimulation, suggesting PMd-cck activation produced an aversive memory. Optogenetic activation of PMd-cck cells also increased pupil size, heart rate and respiration rate (Figure 2G–I). Thus, PMd-activation induced behavioral, psychological and physiological symptoms associated with threat exposure.

**PMd-cck cells encode escape induced by multiple threat modalities**

Our results show PMd-cck activity is necessary and sufficient for escape from numerous threats (Figure 1), suggesting these cells may encode escape. We thus performed one-photon imaging in PMd-cck cells expressing the $Ca^{2+}$ indicator GCaMP6s (Figure 3A–C) to extract activity from PMd-cck cell ensembles (Figure 3D–E). Importantly, the number of escapes observed in mice with microscope implants (Figure 3F) was not different from control un-implanted mice (rat $p$=0.723, heated plate $p$=0.439, $CO_2$ $p$=0.291).

We used a hidden Markov Model (HMM) to identify the two most prominent network states in these data. The HMM was chosen for its simplicity and ability to model the latent processes, or 'hidden states,' of sequential data. As an unsupervised technique, it identifies

states that are strongly represented in the data without using a teaching signal. This method separated different time points of the neural data into distinct states without any input about escapes. The neural data was the only provided input to the model. Remarkably, this method detected ensemble states that were highly predictive of escape occurrence in all three escape assays (Figure 3G–H), indicating that the most prominent state motifs are related to escape behavior. Similar results were found with different methods and parameters, including $k$-means clustering, an unsupervised approach that is arguably simpler than HMM for its exclusion of data sequentiality, and 5-fold logistic regression, one of the simplest supervised modeling methods (Figure S6A–C). These converging results show the findings are robust across model selection and indicate escape-related state encoding is a prominent feature of PMd-cck ensemble activity. Indeed, cells were active both before and after escape in each assay (Figure 3I). Furthermore, a high fraction of cells were significantly activated during escape (Figure 3J). Cells were classified as escape-activated if their weight for escape in a general linear model was higher than expected by chance compared to a bootstrap distribution (see Methods, "Escape cell classification"). These cells were used in Figure 3J–M. Fluorescence traces from these significantly escape-activated cells peaked either before (green) or after (yellow) the onset of escape (Figure 3K–L). Strikingly, the proportion of peaks occurring prior to escape onset was higher for the rat and heated floor assays than during $CO_2$ exposure (Figure 3M). These data demonstrate that PMd-cck cells are engaged more strongly prior to context-specific escapes than to panic-related jumping.

Miniscope-implanted mice did not consistently display climbing in control assays, precluding comparisons of cell activity during climbs in control and threat contexts. PMd activation was not observed during other behaviors, such as running or risk-assessment stretch-attend postures (Figure S6D), showing PMd activation is selectively linked to escape. Lastly, though jumps were more common, a few climbs were seen in the $CO_2$ assay. Forty-seven % of cells activated by climb in $CO_2$ were not activated during jumps. Moreover, exclusive climb-categorized cells tended to exhibit more pre- versus post-escape $Ca^{2+}$ transients than exclusive jump-categorized cells (Fig S6E, right), indicating a population of PMd cells is selectively activated during context-specific escape.

### PMd-cck synchronizes with dlPAG in all escapes and with thalamic amv nucleus only during context-specific escape

We next investigated the PMd-cck outputs that mediate escape. The two main targets of the PMd are the dorsolateral periaqueductal gray (dlPAG) and the anteromedial ventral thalamus (amv) (Canteras and Swanson, 1992). The dlPAG controls escape in general (Del-Ben and Graeff, 2009; Tovote et al., 2016). The amv has head direction cells (Bassett et al., 2007), is involved in spatial navigation and projects to navigation regions such as the entorhinal cortex and subiculum (Jankowski et al., 2013). We thus hypothesized the PMd-dlPAG projection is necessary for all escapes, while the PMd projection to amv is involved in escape requiring spatial navigation, but not in panic-related jumping.

As prior PMd connectivity studies were performed without cell-type specificity, it is unclear if PMd-cck cells project to the dlPAG and amv. Following injection of retrobeads in the dlPAG, 94% of PMd-cck cells were retrogradely labelled (Figure S7A–E). Additionally, in

an *ex vivo* slice preparation, all recorded dlPAG cells (*n*=9) showed glutamatergic monosynaptic glutamatergic excitatory responses following optogenetic stimulation of ChR2-expressing PMd-cck axon terminals (Figure S7F–J). A smaller fraction of PMd cells projected to the amv, and the majority (98%) of amv-projecting PMd cells also projected to the dlPAG (Figure S7K–L). In the PMd, 53% of cells project only to dlPAG and 46% of cells project to both amv and dlPAG (Figure S7M). Thus, there are two major PMd populations: one the projects exclusively to dlPAG and another that projects to both amv and dlPAG.

We next investigated the neural activity of these circuits with dual-site GCaMP6s fiber photometry recordings in the PMd-cck and dlPAG-synapsin cells (Figure 4A–C). These two populations showed increased correlation in activity during exposure to all three threats relative to control stimuli (Figure 4D–F). In contrast, PMd-cck and amv-synapsin activity were more correlated relative to control assays only in the rat and heated floor assays (Figure 4G–K). The correlation between the activity of these two regions had a trending decrease in the $CO_2$ assay (Figure 4K). These data suggest the PMd-cck to dlPAG projection may broadly elicit threat-induced flight. Conversely, functional connectivity in the PMd-cck-amv circuit increases selectively in assays with context-specific escape, but not during panic-induced jumps (Figure 4K), in line with work showing the dlPAG and amv are respectively implicated in initiating escape (Tovote et al., 2016) and in spatial navigation (Jankowski et al., 2013). Activity in all three regions also increased prior to escape during exposure to all threat assays (Figure S8). The slow temporal dynamics of GCaMP did not allow for the identification of a PMd-dlPAG conduction lag, as hypothalamic-PAG lags may be shorter than 15 ms (Behbehani et al., 1988; Sakuma and Pfaff, 1982).

## PMd projection to thalamus is necessary only for context-specific escape, while the projection to dlPAG is required for all escapes

The photometry results (Figure 4F and 4K) indicate that PMd-cck cells projecting to the amv become selectively activated only during context-specific escapes. Conversely, PMd input to the dlPAG may be engaged during all escapes. To test these hypotheses, we recorded $Ca^{2+}$ transients in GCaMP6s-expressing PMd-cck axon terminals (Figure 5A–B). Axons terminating in amv were activated only during the rat and heated plate climb escapes, but not during jumping elicited by $CO_2$. In contrast, axons terminating in the dlPAG were activated during escape in all assays (Figure 5C–D). Furthermore, relative to control assays, PMd-cck axons terminating in the amv displayed larger fluorescence peaks during the rat and heated plate assays, but not the $CO_2$ assay (Figure 5E). In contrast, axons terminating in the dlPAG showed increased activation relative to control assays in all three paradigms (Figure 5E). These data show amv-projecting PMd cells are a population that is selectively activated only during context-specific flight, but not panic-related jumping.

We thus hypothesized that the activity of the PMd cck-dlPAG circuit is broadly necessary for flight, while the PMd-amv projection is specifically necessary for escape requiring spatial navigation. To test these hypotheses, we expressed Arch in PMd-cck cells and delivered green light (532 nm) to PMd-cck Arch-expressing axon terminals in the dlPAG or the amv. Inhibition of the PMd-cck to dlPAG projection (Figure 6A) decreased escape caused by all

threats (Figure 6B). Inhibition of PMd-cck terminals in the amv (Figure 6C) only decreased escape in the rat and heated floor assays (Figure 6D), but did not affect stereotyped jumping in the $CO_2$ assay (Figure 6D). These data indicate that the PMd-dlPAG projection is broadly necessary for escape, while the PMd-amv circuit is selectively engaged during context-specific escape.

## DISCUSSION

We show the PMd is critical for versatile context-specific escape. This skill is crucial for escape that requires coordination of spatial navigation and flight, such as when animals flee a predator in a jungle or humans evacuate a building in flames. The PMd is anatomically well-suited for this role, as it is interconnected with threat detection, escape and navigation-related regions (Canteras and Swanson, 1992; Comoli et al., 2000). Thus, the PMd may detect multiple threat modalities and then induce context-specific escape by engaging spatial navigation nodes.

### PMd induces context-specific escape by engaging thalamic and brainstem outputs

We propose the PMd engages the dlPAG to initiate escape in diverse threatening situations, and that simultaneous engagement of spatial navigation circuits via the amv leads to flexible context-specific flight. However, in the presence of overwhelming threat, the PMd no longer recruits the amv (Figure 4K, 5D and Figure 6D). This difference in PMd functional connectivity may be related to the shift towards panic jumping, despite the presence of a more efficient climbing route that allows longer relief from $CO_2$ (Figure 1I). Indeed, panic induces suboptimal flight (Elliott and Smith, 1993; Helbing et al., 2000; Keating, 1982; Shen et al., 2018).

The unsupervised Hidden Markov method identified a prominent network state in the PMd that predicted escape (Figure 3H). Remarkably, this result could be found by separating the data into only two states, showing that escape-related network states are a key feature of PMd activity. PMd escape-modulated cells also displayed stronger activation prior to context-specific escapes compared to panic-related jumping in $CO_2$ (Figure 3M). These data may indicate that cells related to context-specific escape fire considerably prior to flight onset to provide enough time for downstream circuits to identify optimal escape routes and plan appropriate motor actions. We also observed PMd-cck cell activity peaks after jumps in the $CO_2$ assay (Figure 3K). This activity may be related to controlling escape vigor, as reported for dlPAG cells firing after escape onset (Evans et al., 2018).

Though dlPAG stimulation has analgesic properties, PMd stimulation did not alter analgesia (Figure S2B). PMd excitation may not activate analgesia-mediating endocannabinoid pathways in the dlPAG (Gregg et al., 2012). Indeed, defensive behaviors and analgesia are controlled by separate vlPAG neurons (Tovote et al., 2016).

The PMd is an extremely understudied nucleus, despite providing the densest known input to the panicogenic dlPAG (Del-Ben and Graeff, 2009; Lovick, 2000; Tovote et al., 2016). PMd activation may produce aversion and motivation to escape via the dlPAG, while activation of the amv projection may lead to mobilization of downstream cortical circuits

that integrate contextual cues. This specificity arises because amv-projecting PMd cells, despite also projecting to the dlPAG (Figure S7), are functionally distinct from cells that exclusively project to the dlPAG. Indeed, amv-projecting cells are only active during context-specific escape, but not jumps in $CO_2$, while the projection to dlPAG is active during all escapes (Figure 5). Accordingly, inhibition of the amv projection impaired only context-specific escape, while inhibition of the dlPAG projection decreased flight in general (Figure 6).

Our data show that the PMd does not generate complex flight by its own temporal coding, as the same optogenetic stimulation parameters resulted in different context-specific actions (Figure 2B–C). Instead, downstream circuits likely generated the motor plans for context-specific escapes. The amv may serve these functions by its direct projections to navigation regions such as the entorhinal cortex and action-planning structures such as the secondary motor cortex (Jankowski et al., 2013). Indeed, the amv is necessary for the acquisition of predator-induced contextual fear (Carvalho-Netto et al., 2010), making it a good candidate to coordinate defensive responses associated with spatial memory, such as context-specific escapes. Thus, our data suggest a model according to which PMd activation creates an aversive signal via the dlPAG projection that motivates escape. A context-specific escape is induced only if the amv-projecting PMd cells are also activated, leading to the elaboration of versatile flight motor plans integrating relevant contextual cues to identify and use appropriate escape routes.

### Distributed networks controlling escape

The PMd receives input from a wide variety of sources that support a role for this nucleus in context-specific escape elicited by threats such as predators or $CO_2$. It receives input from other predator-responsive nuclei such as the VMHdm and the anterior hypothalamus and also from $CO_2$-detecting structures such as the orexinergic perifornical region (Comoli et al., 2000). Lastly, the PMd receives connections from the prefrontal cortex, which may provide input related to executive control and also from the nucleus of Gudden, a region critical for contextual memory and spatial navigation (Comoli et al., 2000). Input from these various sources may allow the PMd to detect a wide variety of threats and engage downstream dlPAG and amv outputs to produce appropriate context-specific defensive responses.

We show that inhibition and excitation of PMd-cck cells respectively decreased and increased context-specific and panic-related escape. Interestingly, DMH and VMHdm activation did not elicit context-specific escape climbing (Figure S3). However, these regions control escape in simple environments (Johnson and Shekhar, 2012; Johnson et al., 2008; Wang et al., 2015), indicating that the PMd's ability to mediate both context-specific and panic-related escape may be relatively unique. Indeed, though we activated several hypothalamic regions implicated in escape (Figure S5), only optogenetic stimulation of the PMd caused escape in a novel complex environment (Figure 2C). Electrical dlPAG stimulation (Kim et al., 2013) produced escape to a burrow in the end of a corridor in a simple box. However, optogenetic dlPAG stimulation did not cause escape from the complex upwards step box (Figure S5G), showing that the dlPAG may produce directed escape

provided that the action is relatively simple and does not require sophisticated navigation. Similarly, stimulation of sf1+ VMHdm cells also causes escape and flight (Kunwar et al., 2015; Wang et al., 2015), in agreement with our results showing freezing and jumps during VMHdm stimulation (Figure S3E–G). These cells encode complex environments (Krzywkowski et al., 2020), suggesting they may control complex context-specific escape, as stimulating these cells produces flight towards a hiding area (Wang et al., 2015). Though sf1+ VMHdm stimulation did not consistently produce escape in the upwards step box (Figure S3G), one mouse was able to escape, indicating that direct input from these cells to the PMd may have a role in context-specific escape. Indeed, the VMHdm provides robust input to the PMd (Comoli et al., 2000) and is part of the hypothalamic predator-detection circuit with the PMd (Cezario et al., 2008; Silva et al., 2013), suggesting these two structures have related functions. Perhaps different stimulation parameters may have induced more organized escape following activation of dlPAG or sf1 VMHdm cells.

PMd-mediated escape was seen using numerous threats, different routes and distinct escape motor plans, pointing towards a general role of the PMd in versatile context-specific escape, a vital skill needed to ensure escape and survival from imminent threats (Perusini and Fanselow, 2015). We also report that the PMd recruits both escape-inducing circuits and spatial navigation networks, showing how these two functions are integrated to produce context-specific escape.

## STAR METHODS

### RESOURCE AVAILABILITY

**Lead Contact**—Further information and requests for resources and reagents should be directed to and will be fulfilled by the Lead Contact, Avishek Adhikari (avi@psych.ucla.edu).

**Materials Availability**—This study did not generate new unique reagents.

**Data and code availability**—The datasets generated and/or analyzed in the current study are available from the corresponding author upon reasonable request. All scripts for analyzing data are also available upon reasonable request.

### EXPERIMENTAL MODEL AND SUBJECT DETAILS

All procedures conformed to guidelines established by the National Institutes of Health and have been approved by the University of California, Los Angeles Institutional Animal Care and Use Committee or by the University of Sao Paulo Animal Bioethics committee.

**Mice.**—Cck-IRES-Cre mice (Jackson Laboratory stock No. 012706), SF1-cre (Jackson Laboratory stock No. 012462) and wild type C57BL/6J mice (Jackson Laboratory stock No. 000664) were used for all experiments. Male and female mice between 2 and 6 months of age were used in all experiments. Mice were maintained on a 12-hour reverse light-dark cycle with food and water ad libitum. Sample sizes were chosen based on previous behavioral optogenetics studies on defensive behaviors, which typically use 6–15 mice per group. All mice were handled for a minimum of 5 days prior to any behavioral task.

**Rats.—**Male Long-Evans rats (250–400 grams) were obtained from Charles River Laboratories and were individually housed on a standard 12-hour light-dark cycle and given food and water *ad libitum.* Rats were only used as a predatory stimulus. Rats were handled for several weeks prior to being used and were screened for low aggression to avoid attacks on mice. No attacks on mice were observed in this experiment.

## METHOD DETAILS

### Viral Vectors.

**Optogenetics:** The following adeno-associated viral vectors (AAV), used in the optogenetic experiments, were purchased from Addgene (Watertown, MA): AAV9.hSyn.eGFP.WPRE.bGH, AAV9.Syn.DIO.EGFP.WPRE.hGH, AAV9.hSyn.hChR2. (H134R)-eYFP.WPRE.hGH, AAV9.EF1a.DIO.hChR2(H134R)-eYFP.WPRE.hGH, AAV9-EF1a-DIO-eYFP and AAV9-FLEX-Arch-GFP.

**Chemogenetics:** The following AAVs, used in the chemogenetic experiments, were purchased from Addgene: pAAV8-hSyn-DIO-hM4D(Gi)-mCherry, AAV8.Syn.DIO.HM3D(Gq)-mCherry, and AAV8.Syn.DIO.mCherry.

**Fiber Photometry:** AAV9.Syn.GCaMP6s.WPRE.SV40 and AAV9.Syn.FLEX.GCaMP6s.WPRE.SV40, used in the fiber photometry experiments, were purchased from Addgene.

**Surgeries.:** Surgeries were performed as described previously (Adhikari et al., 2015). Eight-week-old mice were anaesthetized with 1.5–3.0% isoflurane and placed in a stereotaxic apparatus (Kopf Instruments). A scalpel was used to open an incision along the midline to expose the skull. After performing a craniotomy, 40 nl of AAV9.hSyn.hChR2.(H134R)-eYFP.WPRE.hGH at a titer of $2*10^{12}$ particles/ml was injected per site (PMd or other hypothalamic and brainstem nuclei) using a 10 μl nanofil syringe (World Precision Instruments) at 0.08 μl/min. The syringe was coupled to a 33-gauge beveled needle, and the bevel was placed to face the anterior side of the animal. The syringe was slowly retracted 20 minutes after the start of the infusion. Mice received unilateral viral infusion and fiber optic cannula implantation. Infusion locations measured as anterior-posterior, medial-lateral and dorso-ventral coordinates from bregma were: anterior hypothalamus (−0.7, −0.4, −5.2), dorsomedial hypothalamus (−1.94, −0.5, −5.3), ventromedial hypothalamus (−1.5, −0.4, −5.5), lateral hypothalamus (−2.46, −1.1, −5.2) dorsolateral periaqueductal gray (dlPAG) (−4.75, −0.45, −1.9), posterior hypothalamus (−2.30, −0.3, −4.5), dorsal premammillary nucleus (PMd) (−2.46, −0.5, −5.35). For arch experiments and dual photometry assays the dlPAG coordinates were (−4.6, −1.05, −2.1 using a 15-degree angle). Fiber optic cannula (0.22 NA, 200 μm diameter; Doric Lenses) were implanted unilaterally 0.15 mm above the viral infusion sites. Only mice with opsin expression restricted to the intended targets were used for behavioral assays. For optogenetic experiments in PMd-cck mice, the same PMd coordinates were used to inject 0.16 uL of AAV9.EF1a.DIO.hChR2(H134R)-eYFP.WPRE.hGH or AAV9.EF1a.DIO.eYFP.WPRE.hGH. For chemogenetic experiments mice received 0.16 uL of pAAV8-hSyn-DIO-hM4D(Gi)-mCherry, AAV8.Syn.DIO.HM3D(Gq)-mCherry, or AAV8.Syn.DIO. mCherry in the PMd or

dorsomedial hypothalamus coordinates. Similar AAV8-based vectors have been validated and used by numerous other researchers (Hardaway et al., 2019; Jiang-Xie et al., 2019; Shen et al., 2019; Wang et al., 2019).

For photometry experiments mice were injected with 0.16 uL of AAV9.Syn.GCaMP6s.WPRE.SV40 and AAV9.Syn.Flex.GCaMP6s.WPRE.SV40 in the dlPAG and PMd, respectively of cck-cre mice. Mice were implanted unilaterally with cannulae in the PMd and the dlPAG. A 400 μm diameter, 0.48 NA optical fiber (Neurophotometrics) was used for photometry experiments. Adhesive cement (C&B metabond; Parkell, Edgewood, NY, USA) and dental cement (Stoelting, Wood Dale, IL, USA) were used to securely attach the fiber optic cannula to the skull. Half the mice in each cage were randomly assigned to YFP/mcherry or ChR2 /Arch/hM4Di/hM3Dq groups. For miniaturized microscope experiments 40 nL of AAV9-DIO-GCaMP6s was injected in the PMd of cck-cre mice and a GRIN lens was implanted 200 uM above the infusion site. Three weeks following surgery animals were base-plated.

The rats used in this study were obtained from a partner lab and never optogenetically stimulated during the described assays. The rats had fiber optic cannulae implants from prior unrelated experiments. For details of the surgery, see (Malvaez et al.). Briefly, rats were anesthetized with isoflurane and bilaterally infused with AAV5-CaMKIIa-hChR2(H134R)-eYFP or AAV8-CaMKIIa-eYFP. Viral infusion (0.30 μl) was performed at a rate of 6 μl/hr by an infusion needle at the lateral or medial orbitofrontal cortex. Optical fibers (200 μm core, numerical aperture 0.66; Prizmatix, Southfield, MI) positioned in ferrules (Kientec Systems Inc., Stuart, FL) were implanted 0.3 mm above the basolateral amygdala (AP −3.0 mm, ML ± 5.1, DV −7.7).

**In situ hybridization.:** Cck-IRES-Cre mice (Jackson Laboratory stock No. 012706) were euthanized with 5% isoflurane followed by cervical dislocation. Brains were harvested and snap-frozen in 2-methylbutane at −20°C and tissue was sectioned at 18 μm. The workflow was performed in accordance with the manufacturer's protocol for the RNAScope® Multiplex Fluorescent Assay (Advanced Cell Diagnostics, Newark, CA). Riboprobes selective for sequences were labeled as follows: Cre (C1, Cat. No. 312281), nNOS with (437651-C2) and NeuN (Mm-Rbfox3-C3, Cat No. 313311-C3) or VGLUT2 (Mm-Slc17a6-C3, Cat No. 319171-C3). Images were obtained with a Leica DM5500 fluorescent microscope at 40x.

**Immunostaining for NeuN.:** Fixed brains were kept in 30% sucrose at 4oC overnight, and then sectioned on a cryostat (40 μm) slices. Sections were washed in PBS and incubated in a blocking solution (3% normal donkey serum and 0.3% triton-x in PBS) for 1 hour at room temperature. Sections were then incubated at 4oC for 12 hours with polyclonal anti-NeuN antibody made in rabbit (1/500 dilution) (CAT# NBP1-77686SS, Novusbio) in blocking solution. Following primary antibody incubation sections were washed in PBS 3 times for 10 minutes, and then incubated with anti-rabbit IgG (H+L) antibody (1/500 dilution) conjugated to Alexa Fluor 594 (red) (CAT# 8889S, cellsignal.com) for 1 hour at room temperature. Sections were washed in PBS 3 times for 10 minutes, incubated with DAPI

(1/50000 dilution in PBS), washed again in PBS and mounted in glass slides using PVA-DABCO (Sigma).

**Acute brain slice preparation and electrophysiological recordings.:** Acute brain slices preparation and electrophysiological recordings were performed using standard methods as previously described(Nagai et al., 2019).

Briefly, Cck-Cre+ mice that had received AAV microinjections into PMd were deeply anesthetized with isoflurane and decapitated with sharp shears. The brains were placed and sliced in ice-cold modified artificial CSF (aCSF) containing the following (in mM): 194 sucrose, 30 NaCl, 4.5 KCl, 1 $MgCl_2$, 26 $NaHCO_3$, 1.2 NaH2PO4, and 10 D-glucose, saturated with 95% $O_2$ and 5% $CO_2$. A vibratome (DSK-Zero1) was used to cut 300 μm brain sections. The slices were allowed to equilibrate for 30 minutes at 32–34°C in normal aCSF containing (in mM); 124 NaCl, 4.5 KCl, 2 $CaCl_2$, 1 $MgCl_2$, 26 $NaHCO_3$, 1.2 $NaH_2PO_4$, and 10 D-glucose continuously bubbled with 95% $O_2$ and 5% $CO_2$. Slices were then stored at 21–23°C in the same buffer until use. All slices were used within 2–6 hours of slicing.

Slices were placed in the recording chamber and continuously perfused with 95% $O_2$ and 5% $CO_2$ bubbled normal aCSF. pCLAMP10.4 software and a Multi-Clamp 700B amplifier was used for electrophysiology (Molecular Devices). Whole-cell patch-clamp recordings were made from neurons in the PMd or dorsolateral PAG (dlPAG) using patch pipettes with a typical resistance of 4–5 MΩ. Neurons were selected based on reporter fluorescence, i.e. YFP for ChR2-YFP and mCherry for hM3Dq-mCherry or hM4Di-mCherry. The intracellular solution for recordings comprised the following (in mM) : 135 potassium gluconate, 5 KCl, 0.5 $CaCl_2$, 5 HEPES, 5 EGTA, 2 Mg-ATP and 0.3 Na-GTP, pH 7.3 adjusted with KOH. The initial access resistance values were < 20 MΩ for all cells; if this changed by > 20% the cell was discarded. Light flashes (0.2 mW/mm2) from a blue LED light source (Sutter Instruments) were delivered via the microscope optics and a 40x water immersion objective lens and controlled remotely using TTL pulses from Clampex. Cell responses were recorded in whole-cell mode and recorded using an Axopatch 700B amplifier connected via a digitizer to a computer with pCLAMP10 software. To stimulate ChR2 expressed in PMd neurons or axons, 5 ms pulses were delivered at inter-pulse intervals of 200 ms, 50 ms or 25 ms for 5, 20 or 40 Hz optical stimulations, respectively. To assess PMd-dlPAG synaptic transmission, dlPAG neurons in the vicinity of ChR2-expressing PMd axons were patched. To isolate light-evoked EPSCs, neurons were voltage-clamped at −70 mV and pre-incubated with 10 μM bicuculline, an antagonist for $GABA_A$ receptors, for 5 minutes before recording. To block AMPA receptor-mediated EPSCs, 20 μM cyanquixaline (CNQX, 6-cyano-7-nitroquinoxaline-2,3-dione) was applied in the bath. The voltage-gated sodium channel blocker tetrodotoxin (TTX, 0.3 μM) was included in the bath to demonstrate action potential-dependent ChR2-mediated transmitter release. To examine direct (monosynaptic) release of glutamate by PMd axons to dlPAG neurons, EPSCs were measured in the presence of TTX and the voltage-gated K+ channel blocker 4-aminopyridine (4AP, 500 μM) for enhancing ChR2-mediated depolarization of terminals. 5 μM CNO was applied in the bath to stimulate Gq-DREADD hM3Dq or Gi-DREADD

hM4Di expressed in PMd neurons. In some cases, 1 mg/ml biocytin (Tocris, 3349) was added to the intracellular solution to subsequently visualize patched neurons.

**Immunohistochemistry (IHC) for acute sections.:** 300 μm fresh brain slices were placed into 10% buffered formalin overnight at 4°C and processed as follows for IHC. Sections were washed 3 times in 0.1 M PBS with 2% Triton-X 100 for five minutes each, and then incubated in a blocking solution containing 10% NGS in 0.1 M PBS with 1% Triton-X 100 for 1 hr at room temperature with gentle agitation. Sections were then incubated with streptavidin conjugated Alexa 647 (1:250) diluted in 0.1 M PBS with 0.4% Triton-X 100 for overnight at 4°C. The sections were rinsed 3 times in 0.1 M PBS for 10 minutes each before being mounted on microscope slides in fluoromount-G. Images were obtained with the confocal microscopy using a commercial confocal laser scanning microscope (FV1000, Olympus).

**Behavior video capture.:** All behavior videos were captured at 30 frames/sec in standard definition (640×480) using a Logitech HD C310 webcam. To capture fiber-photometry synchronized videos, both the calcium signal and behavior were recorded by the same computer using custom Matlab scripts that also collected timestamp values for each calcium sample/behavioral frame. These timestamps were used to precisely align neural activity and behavior.

**Chemogenetics.:** Mice used for chemogenetic experiments were exposed to each threat and control stimuli twice, once following treatment with saline and once following treatment with CNO (5 mg/kg, injected intraperitoneally) 40 minutes prior to the experiment. Only one control or threat-exposure assay was performed per day with each mouse.

**Rat exposure assay.:** We used a corridor measuring (35 × 20 × 22 cm). At the end of the corridor there is a vertical wall with a wire mesh (with 1 cm x 1 cm square spaces in the mesh). Mice can use the mesh as a ladder to climb the vertical wall (22 cm height) and access a burrow. Mice were acclimated to this environment for three days for 10 minutes. Mice freely explored and independently climbed up the grid ladder. By the end of ten-minute acclimation mice climbed the ladder on their own without being touched by the experimenter's hand. The next day they were exposed either to a toy rat or a live rat for 20 minutes. The rat is restrained to the corner opposite to the mesh grid by a harness attached to a string that is taped to the wall. Mice could climb to avoid the rat and hide in the burrow. After reaching the burrow mice were given 1 minute of hiding time in the burrow. They were then gently placed back in the bottom floor of the context in the same level as the rat (or toy rat). The number of climbs performed during 20 minutes was recorded. This length of 20 minutes includes the 1-minute hiding periods in the burrow.

**Heated floor exposure assay.:** The assay was done on top of a metallic heating plate (14 × 14 cm) (Faithful Magnetic Stirrer model SH-3) that was heated at either 43°C or was at room temperature (20–25°C). A transparent box (14 × 14 × 24 cm) was placed on top of the heated plate. A cylindrical metal mesh was placed that could be used for the mouse to climb to avoid the heat. The mouse was acclimated to this environment for three days (20-minute exposure). The next day the mouse was placed in this environment in either heated or room

temperature floor. Mice climb the cylinder to avoid the heat and then go back to the heated floor as they cannot support their weight while hanging on the cylinder for extended time periods. The number of climbs performed in 20 minutes was measured. We chose 43°C because it is a temperature that caused escape climbs but that is not sufficient to cause pain or skin damage. No pain-related reactions such as paw licking were observed in any of the mice.

**Carbon Dioxide exposure assay.:** Animals were placed in a similar transparent box as the heated floor assay. Mice were acclimated to the environment for three days (10 minutes exposure). The next day mice were exposed either to infusions of air or of 15% $CO_2$. The concentration of $CO_2$ was measured and dynamically adjusted by the ProCO$_2$ 120 controller (Biospherix, Parish, NY, USA) so that $CO_2$ levels are maintained at 15%. This concentration of $CO_2$ elicited escape jumps in all mice tested. The number of escape jumps in 10 minutes was recorded.

**Heated floor pain sensitivity assay.:** We used the same apparatus described for the Heated floor exposure assay above. For this assay the floor was heated at 55°C, which is sufficient to cause pain-related reactions in most mice (paw licking or jumping) within one minute. The latency to display a pain-related reaction was recorded. All mice showed pain responses within 30 seconds.

**Light Delivery for optogenetics.:** For PMd-cck ChR2 mice, blue light was generated by a 473 nm laser (Dragon Lasers, Changchun Jilin, China) at 4.5 mW unless otherwise indicated. Light power was decreased to 2 mW in the nose poke assay to avoid overt escape behaviors. For Figure S7 5 mW was used. For Figure S6G we used 0.5, 2 and 7 mW to test a wide variety of light powers to study dlPAG-induced escape in the upwards step box. Green light was generated by a 532 nm laser (Dragon Lasers), and bilaterally delivered to mice at 10 mW. A Master-8 pulse generator (A.M.P.I., Jerusalem, Israel) was used to drive the blue laser at 20 Hz. This stimulation pattern was used for all ChR2 experiments. The laser output was delivered to the animal via an optical fiber (200 μm core, 0.22 numerical aperture, Doric Lenses, Canada) coupled to the fiberoptic implanted on the animals through a zirconia sleeve.

**Escape from custom-built contexts.:** All measurements are written as length x width x height in cm. In the empty box assay mice were placed in an empty open field ($46 \times 46 \times 36$ cm). Mice were unable to escape from the empty open field as the walls are too high to be jumped over. In the rope climb assay a climbing rope was attached to the same open field used in the empty box assay, connecting the floor to the top of the wall. In the upwards climb assay the rope was removed and an escape path using plastic blocks was placed in the open field. For the rope climb and upwards climb assays the final step in the escape required jumping from the top of the open field (36 cm high) to the floor. For the downwards escape assay blocks were arranged in a staircase-type pattern, and required a jump to exit the last block and land on the floor. The last block was 20 cm higher than the floor. For all escapable assays, a successful escape was recorded only when the mouse was no longer present in the context at the end of 5 minutes. The animals had no habituation, familiarization or training

in any of these assays prior to the experiments. For the inescapable empty box, blue light stimulation to PMd-cck mice expressing cre-dependent YFP or ChR2 was done in alternating 3 minute light ON and OFF epochs for a total of 9 minutes (total of 1 ON and 2 OFF epochs). In all other escape assays, blue light stimulation was done in alternating 30 seconds light ON and OFF epochs (total of five ON and five OFF epochs).

**Nose-poke assay.:** An Arduino board was programmed to trigger 20 Hz 5ms laser trains (473 nm, Dragon Lasers) continuously, unless PMd-cck mice expressing ChR2 nose-poked into a port. Pokes were detected by an infrared beam break sensor (Adafruit, cat# 2168, New York City. NY, USA) that is coupled to the Arduino board. When a beam break occurs due to a nose poke the Arduino board halts triggering laser pulses for 5 seconds. Nose poke times were outputted by the Arduino board to a desktop running Coolterm (https://freeware.the-meiers.org/) to record arduino time point outputs.

**Place aversion test.:** Mice were placed in a two-chamber context $(20 \times 42 \times 27$ cm) for 10 minutes to freely explore the environment. Both chambers are identical. During the next 10 minutes blue light was delivered to the PMd of cck-cre mice expressing either ChR2 or YFP (20 Hz 5ms pulses, 4.5 mW) when they entered one of the chambers. The chamber preferred by the animal during baseline exploration was chosen as the stimulated chamber. Laser stimulation was only delivered during exploration of the simulation chamber. Following 10 minutes of rest in the home cage mice were reintroduced to the context for 10 minutes to measure if PMd stimulation conditioned aversion to the stimulated chamber. The amount of time mice explored both chambers was tracked across all three epochs (baseline, stimulation and post-stimulation epochs).

**Pupil size measurements.:** Pupil size was measured with the same set up and methods described previously (Lovett-Barron et al., 2017). Briefly, a camera (AVT Manta, G-032B) coupled to a24 mm/F1.4 lens was used to image the eye under infrared illumination (Thorlabs M780F2). Video was acquired at 60 Hz using pymba, a Python wrapper for AVT camera control. Frame acquisition times and the behavioral task were synchronized with a National Instruments DAQ (NI PCIe-6323). Pupil size was measured from the video using custom-written Matlab scripts. Each trial lasted 30 seconds. Blue light was delivered to the PMd at 20 Hz, 5ms pulses for 10 seconds following a 10 second baseline recording. Another 10 seconds were recorded post-stimulation.

**Respiratory and heart rate measurements.:** Respiratory rate and heart rate were measured with pulse oximetry as described elsewhere (Adhikari et al., 2015) (MouseOx Plus; Starr Life Sciences, Alllison Park, PA, USA). Data was collected on a computer with MouseOx Plus software. Mice were shaved in the area surrounding the neck and acclimated to moving with the collar sensor used to by the pulse oximeter for four days. Additionally, mice were handled for three days prior to experimenting. Respiratory rate was recorded as a moving average of 10 measurements recorded at 1 Hz. Heart rate was recorded as a moving average of 5 heart beats. Recordings were obtained in head-fixed mice under very light (0.2%) isoflurane anesthesia to avoid motion artifacts in the signal.

**Cat Exposure Test for fos expression.:** The experimental apparatus was made of clear Plexiglas and consisted of a $20 \times 30 \times 40$ cm home cage connected to another $40 \times 30 \times 40$ cm chamber (the food compartment) by a hallway that was 10 cm wide, 25 cm long, and 25 cm high. Between the home cage and the hallway, there was a sliding door that remained closed most of the time, except when the animals were enabled to explore the rest of the apparatus. For 10 days before the cat exposure, each animal was isolated and remained in the home cage. During the middle of the light phase, the home cage door was opened, and the animals were allowed to explore the rest of the apparatus and obtain food pellets stored in the food compartment (habituation). On the 11th day, a neutered 2-year-old male cat was placed and held in the food compartment by an experimenter as the mouse's home cage door was opened, and the animals were exposed for 10 minutes to the cat. Animals exposed to the cat presented clear innate defensive responses: at the beginning of the test, they explored the apparatus, presenting clear risk assessment responses, and the animals immediately fled back to the home cage, where they largely stayed frozen for the remainder of the test. The control group was handled identically as the cat-exposed group, but on the 11th day, the food compartment was empty, and the mice were not exposed to the cat. No food pellets were offered during the test period. Ninety minutes after ending the behavioral testing, the animals were deeply anesthetized with sodium pentobarbital (Cristalia; Itapira, SP, Brazil; 40 mg/kg, i.p.), and the brains were processed for histology and Fos immunohistochemistry

**Rat Exposure Test for fos expression.:** The experimental protocol was very similar to the cat exposure test. In brief, instead of the cat, we used two male adult Long-Evans rats with their bedding in the food compartment. The mice also displayed innate defensive behaviors and they were perfused ninety minutes after ending the behavioral test. Since the behavioral apparatus and procedures were the same for the cat and rat exposure test, the control group (already described) was used as reference for both experimental groups.

**Hypercapnia Test for fos expression.:** For this test, after being habituated during 10 days in the hypercapnia box under room air conditions (0.04% $CO_2$, 21% $O_2$), the mice were submitted to hypercapnia conditions (15% $CO_2$, 21% $O_2$) for 10 minutes. The control group was just exposed to room air conditions. The animals were perfused ninety minutes after the test.

**Fos Immunohistochemistry and Histology.:** Animals were perfused and the brains later frozen and cut on a sliding microtome in the frontal plane. One series of sections was processed for immunohistochemistry with anti-Fos antiserum raised in rabbit (c-fos(Ab-5); EMD Millipore;#PC38) at a dilution of 1:20 000. The primary antiserum was detected using a variation of the avidin—biotin complex system. In brief, sections were incubated for 90 minutes at room temperature in a solution of biotinylated goat antirabbit IgG (Vector Laboratories,#BP-9100) and then placed in the mixed avidin–biotin horseradish peroxidase complex solution (ABC Elite Kit; Vector Laboratories,#PK-6105) for the same period. The peroxidase complex was visualized by a five-minute exposure to a chromogen solution containing 0.02% 3,30 diaminobenzidine tetrahydrochloride (DAB; Sigma) with 0.3% nickel–ammonium sulfate in 0.05 M Tris buffer (pH 7.6) followed by incubation for 20 minutes in chromogen solution with hydrogen peroxide (1:3000), which produced a blue-

black product. The reaction was stopped by extensive washing in 0.02 M KPBS (pH 7.4). Sections were mounted on gelatin-coated slides and then dehydrated and coverslipped with DPX (Sigma). An adjacent series was always stained with thionin to serve as a reference series for cytoarchitectonic purposes.

**Quantification of Fos-Labeled Cells.:** The density of Fos immunoreactive neurons was evaluated by an observer without knowledge of the animal's experimental group. Images were generated for selected regions using the 10x objective of a Nikon Eclipse 80i (Nikon Corporation, ChiyodaKu, Tokyo-To, Japan) microscope equipped with a Nikon digital camera DXM1200F (Nikon Corporation). To quantify the density of Fos labeling, we first delineated the borders of the selected regions in a given section as defined in adjoining Nissl stained sections. Fos-labeled cells were then counted therein. Only darkly labeled oval nuclei that fell within the borders of a region of interest were counted. The density of Fos labeling was determined by dividing the number of Fos-immunoreactive cells by the area of the region of interest. Both cell counting and area measurements were performed with the aid of a computer program (Image-Pro Plus, version 4.5.1; Media Cybernetics, Silver Spring, MD, USA). Cell densities were obtained on both sides of the brain and averaged for each mouse. The brain regions examined in the present investigation followed the Brain Maps: Structure of the Rat Brain.

**Miniscope video capture.:** All videos were recorded at 30 frames/sec using a Logitech HD C310 webcam and custom-built head-mounted UCLA miniscope (Cai et al., 2016). Open-source UCLA Miniscope software and hardware (http://miniscope.org/) were used to capture and synchronize neural and behavioral video (Cai et al., 2016).

**Retrobead tracing.:** Retrobeads (LumaFluor) (30 nL) were injected in the dlPAG diluted 6 times using a 10 μl nanofil syringe (World Precision Instruments) at 40 nl/min. The syringe was coupled to a 33-gauge beveled needle, and the bevel was placed to face the anterior side of the animal. The syringe was slowly retracted 20 minutes after the start of the infusion.

**Fiber photometry.:** Photometry was performed as described in detail previously (Kim et al., 2016). Briefly, we used a 405-nm LED and a 470-nm LED (Thorlabs, M405F1 and M470F1) for the $Ca^{2+}$-dependent and $Ca^{2+}$independent isosbestic control measurements. The two LEDs were band-pass filtered (Thorlabs, FB410–10 and FB470–10) and then combined with a 425-nm long-pass dichroic mirror (Thorlabs, DMLP425R) and coupled into the microscope using a 495-nm long-pass dichroic mirror (Semrock, FF495-Di02–25 ×36). Mice were connected with a branched patch cord (400 μm, Doric Lenses, Quebec, Canada) using a zirconia sleeve to the optical system. The signal was captured at 20 Hz (alternating 405-nm LED and 470-nm LED). To correct for signal artifacts of a non biological origin (i.e. photo-bleaching and movement artifacts), custom Matlab scripts leveraged the reference signal (405-nm), unaffected by calcium saturation, to isolate and remove these effects from the calcium signal (470-nm).

**Perfusion and histological verification.:** Mice were anesthetized with Fatal-Plus and transcardially perfused with phosphate buffered saline followed by a solution of 4% paraformaldehyde. Extracted brains were stored for 12 hs at 4°C in 4% paraformaldehyde.

Brains were then placed in sucrose for a minimum of 24 hs. Brains were sectioned in the coronal plane in a cryostat, washed in phosphate buffered saline and mounted on glass slides using PVA-DABCO. Images were acquired using a Keyence BZ-X fluorescence microscope with a 10 or 20X air objective.

## QUANTIFICATION AND STATISTICAL ANALYSIS

**Behavioral quantification.—**To extract the pose of freely-behaving mice in the described assays, we implemented DeepLabCut (Nath et al., 2019), an open-source convolutional neural network-based toolbox, to identify mouse nose, ear and tail base xy-coordinates in each recorded video frame. These coordinates were then used to calculate velocity and position at each timepoint, as well as classify behaviors such as climbs, jumps, escape runs and freezes in an automated manner using custom Matlab scripts. Specifically:

**Rat Assay:** 'Climbs' were classified as epochs for which (1) the vertical speed of the mouse nose and tail base exceeded 2 cm/s, as this threshold correctly identified all empirically observed climbs, and (2) the start and end points of these epochs, defined by mouse nose coordinates, were respectively below and above an experimenter-defined climbing area bounding box.

'Escape runs' were defined as epochs for which (1) the mouse was not located in the upper burrow or ladder area and (2) the mouse speed away from the rat or toy rat exceeded 2 cm/s. As there was little room for acceleration between the rat and opposite wall, the speed threshold was set to this relatively low value.

'Stretch-attend postures' were defined as epochs for which (1) the distance between mouse nose and tail base exceeded a distance of approximately 1.2 mouse body lengths and (2) mouse tail base speed fell below 1 cm/s.

**Heated Plate and $CO_2$:** 'Climbs' were identified as epochs for which (1) the vertical speed of the mouse nose and tail base coordinates both exceeded 2 cm/s within an experimenter-defined cylindrical mesh bounding box, and fell below 10 cm/s to exclude higher velocity jumps, and (2) the start and end points of these epochs, defined by mouse nose and tail base coordinates, were respectively below and above the lower edge of this bounding box.

**$CO_2$:** 'Jumps' were identified as epochs for which (1) the vertical speed of the mouse nose and tail base exceeded 15 cm/s and (2) the start and end points of these epochs, defined by mouse nose and tail base coordinates, were respectively below and above an experimenter-defined bounding box of the enclosure floor.

**All assays:** 'Pauses' were defined as periods for which mouse tail base speed fell below 1 cm/s for at least 0.33 s.

'Freezes' were defined as periods for which mouse nose and tail base speed fell below 0.25 cm/s for at least 0.33 s (Schuette et al., 2020).

All behaviors were manually checked by the experimenters for error.

**Miniscope postprocessing.**—The open-source UCLA miniscope analysis package (https://github.com/daharoni/Miniscope_Analysis) (Aharoni and Hoogland, 2019) was used to motion correct miniscope videos. They were then temporally down sampled by a factor of four and spatially down sampled by a factor of two. The cell activity and footprints were extracted using the open-source package Constrained Nonnegative Matrix Factorization for microEndoscopic data (CNMF-E; https://github.com/zhoupc/CNMF_E) (Schuette et al., 2020; Zhou et al., 2018). Only cells whose variance was greater than or equal to 25% of the maximum variance among non-outliers were used in the analysis.

**Neural state identification.**—A Hidden Markov Model (HMM) was used to identify escape-related states from the neural data in an unsupervised manner (For the code, see 'Expectation-Maximization for HMMs using real-values Gaussian observations' at Zoubin Ghahramani's code base: http://mlg.eng.cam.ac.uk/zoubin/software.html). This unsupervised approach identifies 'hidden states,' or states that are strongly represented in the neural data, without any additional information about animal behavior. We implemented the model by specifying either two or six of these 'hidden states.' The state with the most corresponding escapes was labelled the 'escape state.' All sessions for each assay were concatenated, and accuracy was calculated as the percent of escape indices to co-occur with this escape state. To determine chance level, we built a bootstrapped distribution of accuracies (1000 iterations), randomly selecting indices (the same number as escape indices) and calculating the percent that co-occurred with the escape cluster by chance. Chance level was defined as the 95th percentile of the resulting distribution.

To determine whether the HMM results agree with those of other unsupervised techniques, we also implemented k-means clustering to identify escape-related clusters in the neural data. We used the *k*-means algorithm (*k*=2) to cluster the top principal components of the neural data (accounting for >=80% of the total variance). The escape cluster, escape prediction accuracy, and chance accuracy were calculated as described above for the HMM analysis.

**Behavior decoding using PMd neural data.**—Discrete classification of escape behavior was performed using multinomial logistic regression. Timepoints preceding and following escape by 5 seconds were labelled 'escape,' and a matched number of non-escape timepoints were randomly selected for training and validation. Each time point was treated as an individual data point. Training and validation were performed using 5-fold cross-validation, with a minimum of 5 seconds between training and validation sets. As equal numbers of escape and non-escape samples were used to build the training and validation sets, chance accuracy was 50%. Sessions with less than 5 escapes were excluded from the analysis.

**Escape cell classification.**—To classify PMd cells as escape-encoding (specifically, climbs in the rat and heated plate assay and jumps in 15% $CO_2$), we used a generalized linear model (GLM) to identify cells that showed increased calcium activity during escape behavior. We fit this model to each cell's activity, with escape indices as the predictor variable and escape coefficient as the measure of fit. Escape onset times were then randomized 100 times and a bootstrap distribution built from the resulting GLM coefficients.

A cell was considered an escape cell if its coefficient exceeded 95% of the bootstrap coefficient values.

**Calcium peak identification.—**For calcium data preceding and following escape by 10 seconds, peaks were identified as samples that were larger than their neighboring samples by a specified amount (Matlab function 'findpeaks' with 'MinPeakProminence' set to 0.4).

**Dual photometry correlation analysis.—**The nonparametric Spearman method was used to correlate the session length PMd/dlPAG and PMd/amv fiber photometry signals in threat and control assays.

**Statistics.—**Two-way repeated measures ANOVA was used, followed by Wilcoxon rank-sum post-hoc tests, unless otherwise stated. Two-tailed tests were used throughout with $\alpha=0.05$. Variance equality was tested using the F-test. Asterisks in the Figure s indicate the *p* values for the post-hoc test. Standard error of the mean was plotted in each Figure as an estimate of variation. Multiple comparisons were adjusted with the false discovery rate method. See complete statistical data for all Figures on Supplementary Table S1.

## Supplementary Material

Refer to Web version on PubMed Central for supplementary material.

## ACKNOWLEDGEMENTS

## REFERENCES

Adhikari A, Lerner TN, Finkelstein J, Pak S, Jennings JH, Davidson TJ, Ferenczi E, Gunaydin LA, Mirzabekov JJ, Ye L, et al. (2015). Basomedial amygdala mediates top-down control of anxiety and fear. Nature 527, 179–185. [PubMed: 26536109]

Aguiar DC, and Guimaraes FS (2009). Blockade of NMDA receptors and nitric oxide synthesis in the dorsolateral periaqueductal gray attenuates behavioral and cellular responses of rats exposed to a live predator. J. Neurosci. Res. 87, 2418–2429. [PubMed: 19360885]

Aharoni D, and Hoogland TM (2019). Circuit Investigations With Open-Source Miniaturized Microscopes: Past, Present and Future. Front. Cell. Neurosci. 13, 141. [PubMed: 31024265]

Bassett JP, Tullman ML, and Taube JS (2007). Lesions of the tegmentomammillary circuit in the head direction system disrupt the head direction signal in the anterior thalamus. J. Neurosci. 27, 7564–7577. [PubMed: 17626218]

Behbehani MM, Park MR, and Clement ME (1988). Interactions between the lateral hypothalamus and the periaqueductal gray. J. Neurosci. 8, 2780–2787. [PubMed: 2900881]

Blanchard DC, Griebel G, and Blanchard RJ (2001). Mouse defensive behaviors: pharmacological and behavioral assays for anxiety and panic. Neurosci. Biobehav. Rev. 25, 205–218. [PubMed: 11378177]

Blank DA (2018). Escaping behavior in goitered gazelle. Behavioural Processes 147, 38–47. [PubMed: 29274760]

Cai DJ, Aharoni D, Shuman T, Shobe J, Biane J, Song W, Wei B, Veshkini M, La-Vu M, Lou J, et al. (2016). A shared neural ensemble links distinct contextual memories encoded close in time. Nature 534, 115–118. [PubMed: 27251287]

Canteras NS, and Swanson LW (1992). The dorsal premammillary nucleus: an unusual component of the mammillary body. Proc. Natl. Acad. Sci. U. S. A. 89, 10089–10093. [PubMed: 1279669]

Carvalho-Netto EF, Martinez RCR, Baldo MVC, and Canteras NS (2010). Evidence for the thalamic targets of the medial hypothalamic defensive system mediating emotional memory to predatory threats. Neurobiol. Learn. Mem. 93, 479–486. [PubMed: 20096798]

Cezario AF, Ribeiro-Barbosa ER, Baldo MVC, and Canteras NS (2008). Hypothalamic sites responding to predator threats--the role of the dorsal premammillary nucleus in unconditioned and conditioned antipredatory defensive behavior. Eur. J. Neurosci. 28, 1003–1015. [PubMed: 18691328]

Chan KY, Jang MJ, Yoo BB, Greenbaum A, Ravi N, Wu WL, Sánchez-Guardado L, Lois C, Mazmanian SK, Deverman BE, Gradinaru V. Engineered AAVs for efficient noninvasive gene delivery to the central and peripheral nervous systems. Nat Neurosci. 2017 8; 20(8):1172–1179. [PubMed: 28671695]

Chen TW, Wardill TJ, Sun Y, Pulver SR, Renninger SL, Baohan A, Schreiter ER, Kerr RA, Orger MB, Jayaraman V, Looger LL, Svoboda K, Kim DS. Ultrasensitive fluorescent proteins for imaging neuronal activity. Nature. 2013 7 18;499(7458):295–300. [PubMed: 23868258]

Chou X-L, Wang X, Zhang Z-G, Shen L, Zingg B, Huang J, Zhong W, Mesik L, Zhang LI, and Tao HW (2018). Inhibitory gain modulation of defense behaviors by zona incerta. Nat. Commun. 9, 1151. [PubMed: 29559622]

Chow BY, Han X, Dobry AS, Qian X, Chuong AS, Li M, Henninger MA, Belfort GM, Lin Y, Monahan PE, Boyden ES. High-performance genetically targetable optical neural silencing by light-driven proton pumps. Nature. 2010 1 7;463(7277):98–102. [PubMed: 20054397]

Comoli E, Ribeiro-Barbosa ER, and Canteras NS (2000). Afferent connections of the dorsal premammillary nucleus. J. Comp. Neurol. 423, 83–98. [PubMed: 10861538]

Del-Ben CM, and Graeff FG (2009). Panic Disorder: Is the PAG Involved? Neural Plasticity 2009, 1–9.

Deng H, Xiao X, and Wang Z (2016). Periaqueductal Gray Neuronal Activities Underlie Different Aspects of Defensive Behaviors. J. Neurosci. 36, 7580–7588. [PubMed: 27445137]

Elliott D, and Smith D (1993). Football stadia disasters in the United Kingdom: learning from tragedy? Industrial & Environmental Crisis Quarterly 7, 205–229.

Evans DA, Vanessa Stempel A, Vale R, Ruehle S, Lefler Y, and Branco T (2018). A synaptic threshold mechanism for computing escape decisions. Nature 558, 590–594. [PubMed: 29925954]

Gregg LC, Jung K-M, Spradley JM, Nyilas R, Suplita RL 2nd, Zimmer A, Watanabe M, Mackie K, Katona I, Piomelli D, et al. (2012). Activation of type 5 metabotropic glutamate receptors and diacylglycerol lipase-α initiates 2-arachidonoylglycerol formation and endocannabinoid-mediated analgesia. J. Neurosci. 32, 9457–9468. [PubMed: 22787031]

Hardaway JA, Halladay LR, Mazzone CM, Pati D, Bloodgood DW, Kim M, Jensen J, DiBerto JF, Boyt KM, Shiddapur A, et al. (2019). Central Amygdala Prepronociceptin-Expressing Neurons Mediate Palatable Food Consumption and Reward. Neuron 102, 1088. [PubMed: 31170393]

Hedenstrom A, and Rosén M (2001). Predator versus prey: on aerial hunting and escape strategies in birds. Behav. Ecol. 12, 150–156.

Heithaus MR, Wirsing AJ, Burkholder D, Thomson J, and Dill LM (2009). Towards a predictive framework for predator risk effects: the interaction of landscape features and prey escape tactics. J. Anim. Ecol. 78, 556–562. [PubMed: 19076259]

Helbing D, Farkas I, and Vicsek T (2000). Simulating dynamical features of escape panic. Nature 407, 487–490. [PubMed: 11028994]

Jankowski MM, Ronnqvist KC, Tsanov M, Vann SD, Wright NF, Erichsen JT, Aggleton JP, and O'Mara SM (2013). The anterior thalamus provides a subcortical circuit supporting memory and spatial navigation. Frontiers in Systems Neuroscience 7.

Jiang-Xie L-F, Yin L, Zhao S, Prevosto V, Han B-X, Dzirasa K, and Wang F (2019). A Common Neuroendocrine Substrate for Diverse General Anesthetics and Sleep. Neuron 102, 1053–1065.e4. [PubMed: 31006556]

Johnson PL, and Shekhar A (2012). An animal model of panic vulnerability with chronic disinhibition of the dorsomedial/perifornical hypothalamus. Physiology & Behavior 107, 686–698. [PubMed: 22484112]

Johnson PL, Truitt WA, Fitz SD, Lowry CA, and Shekhar A (2008). Neural Pathways Underlying Lactate-Induced Panic. Neuropsychopharmacology 33, 2093–2107. [PubMed: 18059441]

Johnson PL, Fitz SD, Hollis JH, Moratalla R, Lightman SL, Shekhar A, and Lowry CA (2011). Induction of c-Fos in "panic/defence"-related brain circuits following brief hypercarbic gas exposure. Journal of Psychopharmacology 25, 26–36. [PubMed: 20080924]

Keating JP (1982). The myth of panic. Fire J. 147, 57–61.

Kim CK, Yang SJ, Pichamoorthy N, Young NP, Kauvar I, Jennings JH, Lerner TN, Berndt A, Lee SY, Ramakrishnan C, et al. (2016). Simultaneous fast measurement of circuit dynamics at multiple sites across the mammalian brain. Nat. Methods 13, 325–328. [PubMed: 26878381]

Kim EJ, Horovitz O, Pellman BA, Tan LM, Li Q, Richter-Levin G, and Kim JJ (2013). Dorsal periaqueductal gray-amygdala pathway conveys both innate and learned fear responses in rats. Proc. Natl. Acad. Sci. U. S. A. 110, 14795–14800. [PubMed: 23959880]

Kobes M, Helsloot I, de Vries B, and Post JG (2010). Building safety and human behaviour in fire: A literature review. Fire Saf. J. 45, 1–11.

Kragel PA, Bianciardi M, Hartley L, Matthewson G, Choi J-K, Quigley KS, Wald LL, Wager TD, Feldman Barrett L, and Satpute AB (2019). Functional Involvement of Human Periaqueductal Gray and Other Midbrain Nuclei in Cognitive Control. J. Neurosci. 39, 6180–6189. [PubMed: 31160537]

Krashes MJ, Koda S, Ye C, Rogan SC, Adams AC, Cusher DS, Maratos-Flier E, Roth BL, Lowell BB. Rapid, reversible activation of AgRP neurons drives feeding behavior in mice. J Clin Invest. 2011 4;121(4):1424–8. [PubMed: 21364278]

Krzywkowski P, Penna B, and Gross CT (2020). Dynamic encoding of social threat and spatial context in the hypothalamus. Elife 9.

Kunwar PS, Zelikowsky M, Remedios R, Cai H, Yilmaz M, Meister M, and Anderson DJ (2015). Ventromedial hypothalamic neurons control a defensive emotion state. Elife 4.

Lecca S, Meye FJ, Trusel M, Tchenio A, Harris J, Schwarz MK, Burdakov D, Georges F, and Mameli M (2017). Aversive stimuli drive hypothalamus-to-habenula excitation to promote escape behavior. eLife 6.

Li Y, Zeng J, Zhang J, Yue C, Zhong W, Liu Z, Feng Q, and Luo M (2018). Hypothalamic Circuits for Predation and Evasion. Neuron 97, 911–924.e5. [PubMed: 29398361]

Lovett-Barron M, Andalman AS, Allen WE, Vesuna S, Kauvar I, Burns VM, and Deisseroth K (2017). Ancestral Circuits for the Coordinated Modulation of Brain State. Cell 171, 1411–1423.e17. [PubMed: 29103613]

Lovick TA (2000). Panic Disorder-A Malfunction of Multiple Transmitter Control Systems within the Midbrain Periaqueductal Gray Matter? Neuroscientist 6, 48–59.

Malvaez M, Shieh C, Murphy MD, Greenfield VY, and Wassum KM Distinct cortical-amygdala projections drive reward value encoding and retrieval.

Martinez RCR, Carvalho-Netto EF, Amaral VCS, Nunes-de-Souza RL, and Canteras NS (2008). Investigation of the hypothalamic defensive system in the mouse. Behavioural Brain Research 192, 185–190. [PubMed: 18468701]

Nagai J, Rajbhandari AK, Gangwani MR, Hachisuka A, Coppola G, Masmanidis SC, Fanselow MS, and Khakh BS (2019). Hyperactivity with Disrupted Attention by Activation of an Astrocyte Synaptogenic Cue. Cell 177, 1280–1292.e20. [PubMed: 31031006]

Nath T, Mathis A, Chen AC, Patel A, Bethge M, and Mathis MW (2019). Using DeepLabCut for 3D markerless pose estimation across species and behaviors. Nat. Protoc. 14, 2152–2176. [PubMed: 31227823]

Perusini JN, and Fanselow MS (2015). Neurobehavioral perspectives on the distinction between fear and anxiety. Learn. Mem. 22, 417–425. [PubMed: 26286652]

Sakuma Y, and Pfaff DW (1982). Properties of ventromedial hypothalamic neurons with axons to midbrain central gray. Exp. Brain Res. 46, 292–300. [PubMed: 6284542]

Schuette PJ, Reis FMCV, Maesta-Pereira S, Chakerian M, Torossian A, Blair GJ, Wang W, Blair HT, Fanselow MS, Kao JC, et al. (2020). Long-Term Characterization of Hippocampal Remapping during Contextual Fear Acquisition and Extinction. J. Neurosci. 40, 8329–8342. [PubMed: 32958567]

Shang C, Chen Z, Liu A, Li Y, Zhang J, Qu B, Yan F, Zhang Y, Liu W, Liu Z, et al. (2018). Divergent midbrain circuits orchestrate escape and freezing responses to looming stimuli in mice. Nature Communications 9.

Shen J, Wang D, Wang X, Gupta S, Ayloo B, Wu S, Prasad P, Xiong Q, Xia J, and Ge S (2019). Neurovascular Coupling in the Dentate Gyrus Regulates Adult Hippocampal Neurogenesis. Neuron 103, 878–890.e3. [PubMed: 31257104]

Shen J-Q, Wang X-W, and Jiang L-L (2018). The influence of panic on the efficiency of escape. Physica A: Statistical Mechanics and Its Applications 491, 613–618.

Silva BA, Mattucci C, Krzywkowski P, Murana E, Illarionova A, Grinevich V, Canteras NS, Ragozzino D, and Gross CT (2013). Independent hypothalamic circuits for social and predator fear. Nat. Neurosci. 16, 1731–1733. [PubMed: 24212674]

Silva BA, Mattucci C, Krzywkowski P, Cuozzo R, Carbonari L, and Gross CT (2016). The ventromedial hypothalamus mediates predator fear memory. Eur. J. Neurosci. 43, 1431–1439. [PubMed: 26991018]

Tovote P, Esposito MS, Botta P, Chaudun F, Fadok JP, Markovic M, Wolff SBE, Ramakrishnan C, Fenno L, Deisseroth K, et al. (2016). Midbrain circuits for defensive behaviour. Nature 534, 206–212. [PubMed: 27279213]

Wang L, Chen IZ, and Lin D (2015). Collateral pathways from the ventromedial hypothalamus mediate defensive behaviors. Neuron 85, 1344–1358. [PubMed: 25754823]

Wang TA, Teo CF, Åkerblom M, Chen C, Tynan-La Fontaine M, Greiner VJ, Diaz A, McManus MT, Jan YN, and Jan LY (2019). Thermoregulation via Temperature-Dependent PGD2 Production in Mouse Preoptic Area. Neuron 103, 349. [PubMed: 31319050]

Woodbury PB (1986). The geometry of predator avoidance by the blue crab, Callinectes sapidus Rathbun. Anim. Behav. 34, 28–37.

Xiong XR, Liang F, Zingg B, Ji X-Y, Ibrahim LA, Tao HW, and Zhang LI (2015). Auditory cortex controls sound-driven innate defense behaviour through corticofugal projections to inferior colliculus. Nature Communications 6.

Zhou P, Resendez SL, Rodriguez-Romaguera J, Jimenez JC, Neufeld SQ, Giovannucci A, Friedrich J, Pnevmatikakis EA, Stuber GD, Hen R, et al. (2018). Efficient and accurate extraction of in vivo calcium signals from microendoscopic video data. Elife 7.

## Highlights

The dorsal premammillary nucleus (PMd) controls versatile and panic-related flight.

The hypothalamic PMd nucleus recruits thalamic targets for escapes requiring navigation.

The PMd engages brainstem targets for both context-specific and panic-related escapes.

Other defense-related hypothalamic nuclei only control simple flight actions in mice.
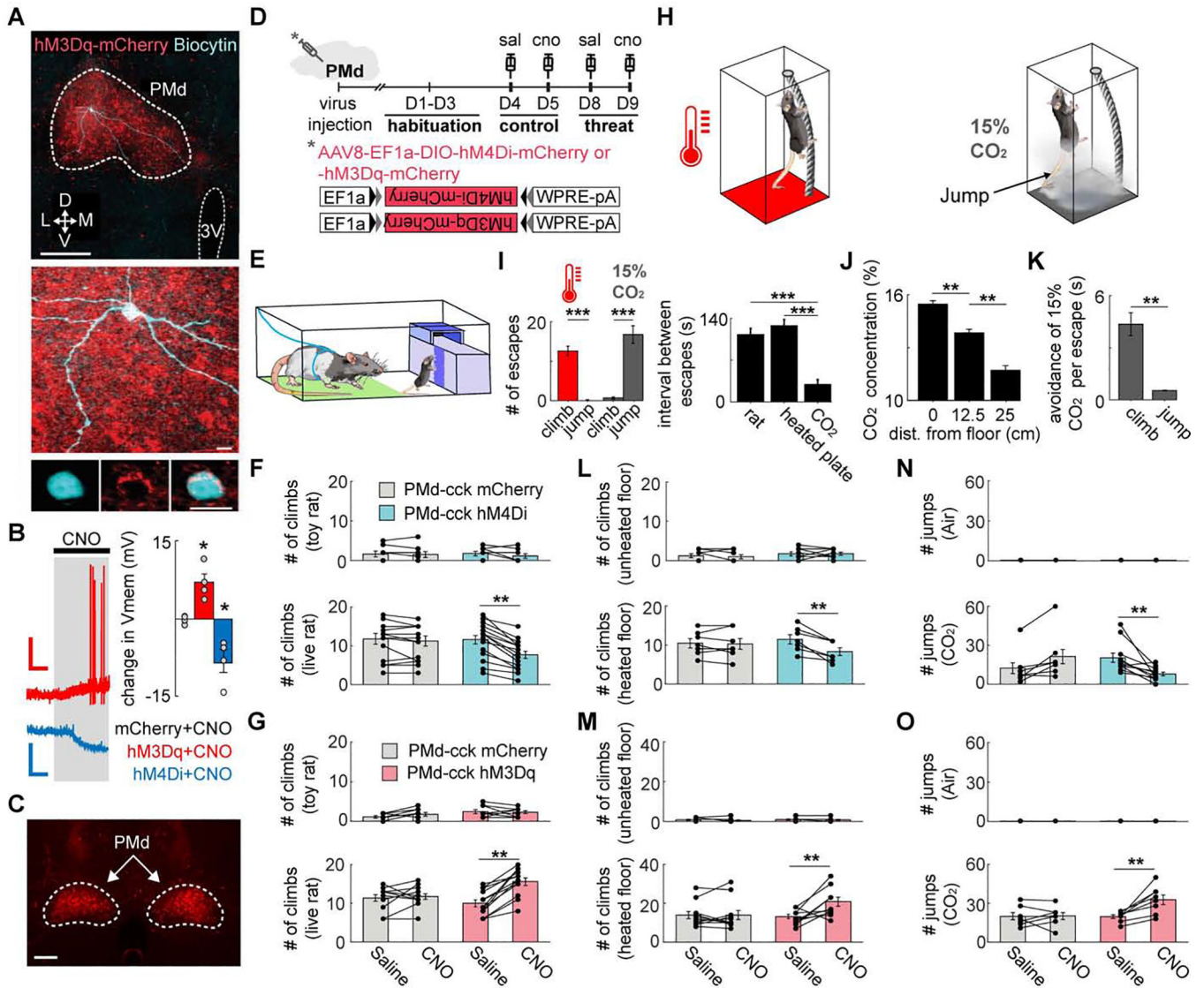
**Figure 1. PMd-cck cells are necessary and sufficient to control context-specific and panic-related stereotyped escape.**

(A) *Ex vivo* slices with cholecystokinin (cck) positive dorsal premammillary nucleus (PMd) cells expressing hM3Dq or hM4Di. Image shows biocytin-filled PMd-cck neuron (blue) and hM3Dq (red). (top scale bar: 200 μm; bottom scale bars: 10 μm)

(B) (left) PMd-cck cells expressing hM3Dq and hM4Di receptors respectively de- and hyperpolarize with clozapine-N-oxide (CNO, 5μM). Scale bars: (red) 60s, 20 mV, (blue) 60s, 10 mV. (right) Average changes in membrane potential following CNO treatment. (mCherry n=4; hM3Dq n=4; hM4Di n=4 cells, 2 cells per mouse; one-way ANOVA followed by Tukey's test, *p<0.05)

(C) Expression of hM4Dq-mcherry in PMd-cck cells for a mouse used in behavioral assays. (scale bar: 200 μm)

(D) Timeline for each DREADD assay.

(E) Rat assay scheme: mice were placed in the presence of an awake rat, restrained by harness to the green area. To escape, mice located and climbed a ladder (dark purple) to

access a burrow. After 1 minute, mice were gently pushed towards the bottom of the ladder. The number of climbs in 20 minutes was counted.

(F) Climbs away from toy rat (top) (mCherry $n=7$, hM4Di $n=7$) or live rat (bottom) (mCherry $n=14$, hM4Di $n=16$) for mice expressing mCherry or hM4Di in PMd-cck cells following treatment with saline or CNO.

(G) Same as (F), but for mice expressing mCherry or hM3Dq in PMd-cck cells. (toy rat: mCherry $n=11$, hM3Dq $n=11$; rat: mCherry $n=12$, hM3Dq $n=13$) (F,G) Chemogenetic PMd-cck inhibition and excitation respectively decreased and increased the number of escapes from rat (Two-way repeated measures ANOVA followed by Wilcoxon test, $**p < 0.01$).

(H) Schemes for heated floor and $CO_2$ assays. (heated floor, left) Mice climbed a cylindrical mesh to escape a 43°C floor, returning to the floor spontaneously. ($CO_2$, right) Mice jumped in the presence of 15% $CO_2$.

(I) (left) Mice climbed more from the heated floor and jumped more in $CO_2$ (heated plate $n=18$; $CO_2$ $n=18$, Wilcoxon signed-rank test). (right) Mean interval between escapes for all assays for saline YFP sessions (rat $n=27$, heated plate $n=17$, $CO_2$ $n=14$).

(J) $CO_2$ concentration decreases with distance from the floor ($n=5$, Wilcoxon signed-rank test).

(K) Bars show the avoidance duration for the 15% $CO_2$ assay for each escape behavior (climb and jump respectively $n=7$ and $n=9$, Wilcoxon signed-rank test).

(L) Climbs away from unheated (top) (mCherry $n=8$, hM4Di $n=8$) or heated floor (bottom) (mCherry $n=7$, hM4Di $n=7$) during 20 minutes in mice expressing mCherry or hM4Di in PMd-cck cells following treatment with saline or CNO.

(M) Same as (L), but for mice expressing mCherry or hM3Dq in PMd-cck cells (unheated floor: mCherry $n=9$, hM3Dq $n=9$; heated floor: mCherry $n=11$, hM3Dq $n=11$).

(N) Number of jumps in 10 minutes for the same groups as in (l) during exposure to air (top) (mCherry $n=9$, hM4Di $n=9$) or carbon dioxide (bottom) (mCherry $n=7$, hM4Di $n=11$).

(O) Number of jumps for the same groups as in (N) during exposure to air (top) or $CO_2$ (bottom) (Air: mCherry $n=9$, hM3Dq $n=9$; $CO_2$: mCherry $n=7$, hM3Dq $n=8$). (B, F-G, I-O) Mean ± SEM.
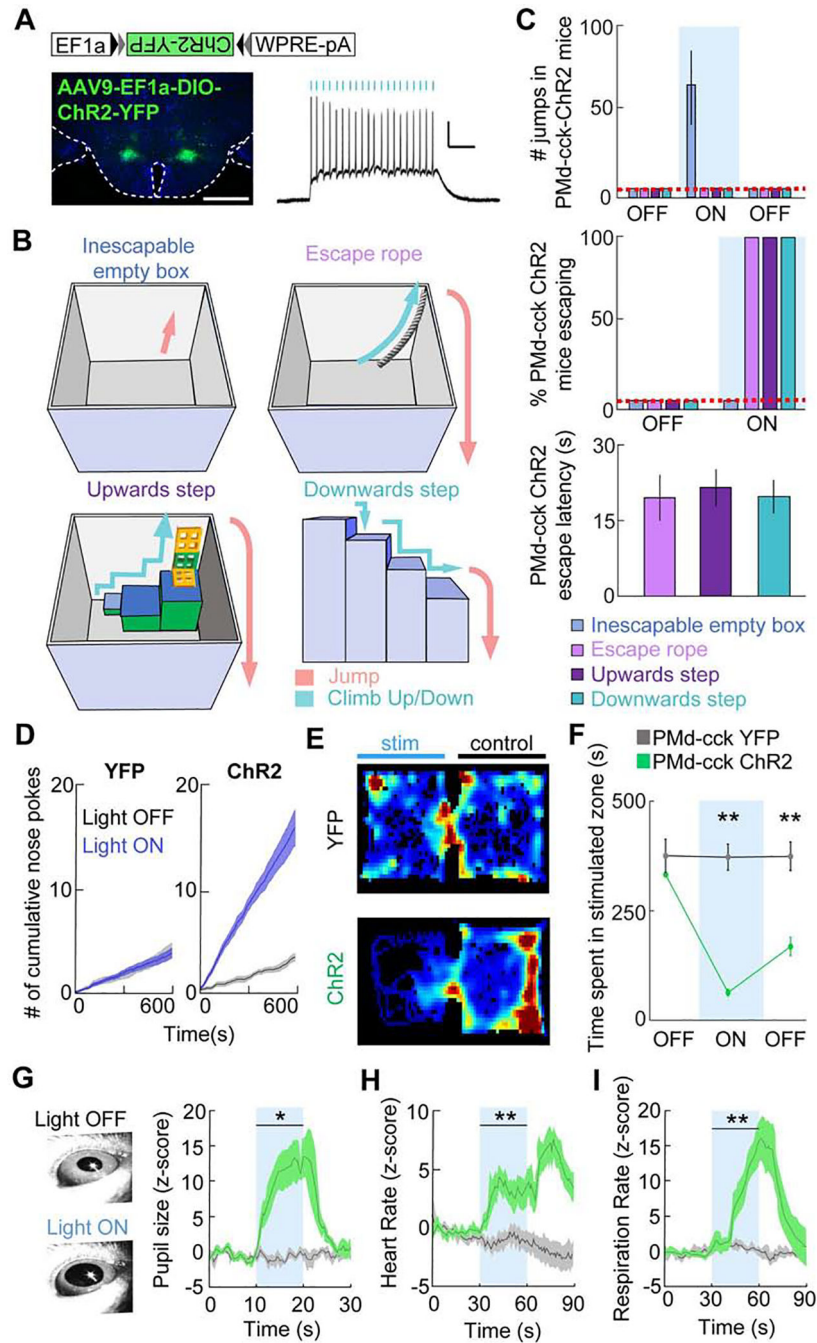
**Figure 2. Optogenetic activation of PMd-cck cells induces versatile context-specific escape from complex environments as well as autonomic activation and aversion.**

(A) Left: Expression of ChR2-YFP in PMd-cck cells. Scale bar: 1 mm. Right: *Ex vivo* recording showing the response of a ChR2-expressing PMd cell to a 20 Hz, 5 ms, 473 nm light train. Scale bar: 2 mV, 0.2 s.

(B) Schemes showing different novel environments in which PMd-cck cells were optogenetically stimulated without any prior training or habituation.

(C) (Upper panel) Number of jumps displayed during optogenetic PMd-cck stimulation in each environment. (Middle panel) Bar graph showing escape success from each of the

environments (Mean±SEM) in (B) following PMd-cck optogenetic activation. During blue light delivery PMd-cck-ChR2 mice jumped to escape in an inescapable empty box. Optogenetic stimulation of the same mice induced escape using the various escape pathways when they were provided, showing PMd-cck activation induced context-specific escape. (Bottom panel) Bar graph showing the escape latency from light-on for PMd-cck ChR2 mice. All mice escaped within the first 30-second stimulation epoch (n=4).

(D) Blue light stimulation was delivered to the PMd continuously and was interrupted for 5 seconds each time the animal nose-poked in a port. PMd-cck-ChR2 mice nose-poked more times than -YFP mice to stop blue light delivery to the PMd, indicating PMd-cck stimulation was aversive (YFP $n$=4, ChR2 $n$=4; Wilcoxon rank-sum test, $p < 0.001$).

(E) Example heat maps showing occupancy of mice expressing either YFP (top) or ChR2-YFP (bottom) in PMd-cck cells in a real-time place preference task.

(F) Average data showing occupancy of the stimulated chamber during baseline, stimulation and post-stimulation periods (respectively labeled OFF, ON and OFF). Each epoch lasted 10 minutes. The post-stimulation period occurred 10 minutes after the end of the stimulation period. Optogenetic stimulation of PMd-cck cells caused marked avoidance of the stimulated chamber during simulation and post-stimulation periods (YFP $n$=8, ChR2 $n$=8; Two-way repeated measures ANOVA followed by Wilcoxon test, **$p < 0.001$ for stimulation / post stimulation epochs).

(G-I) Pupil size, heart rate and respiration rate in head-fixed mice increased during blue light delivery to PMd-cck-ChR2, but not YFP mice (YFP $n$=4, ChR2 $n$=4; Two-way repeated measures ANOVA followed by Wilcoxon test, *$p < 0.05$, ** $p < 0.01$). (C,D,F,G-I) Mean ± SEM.
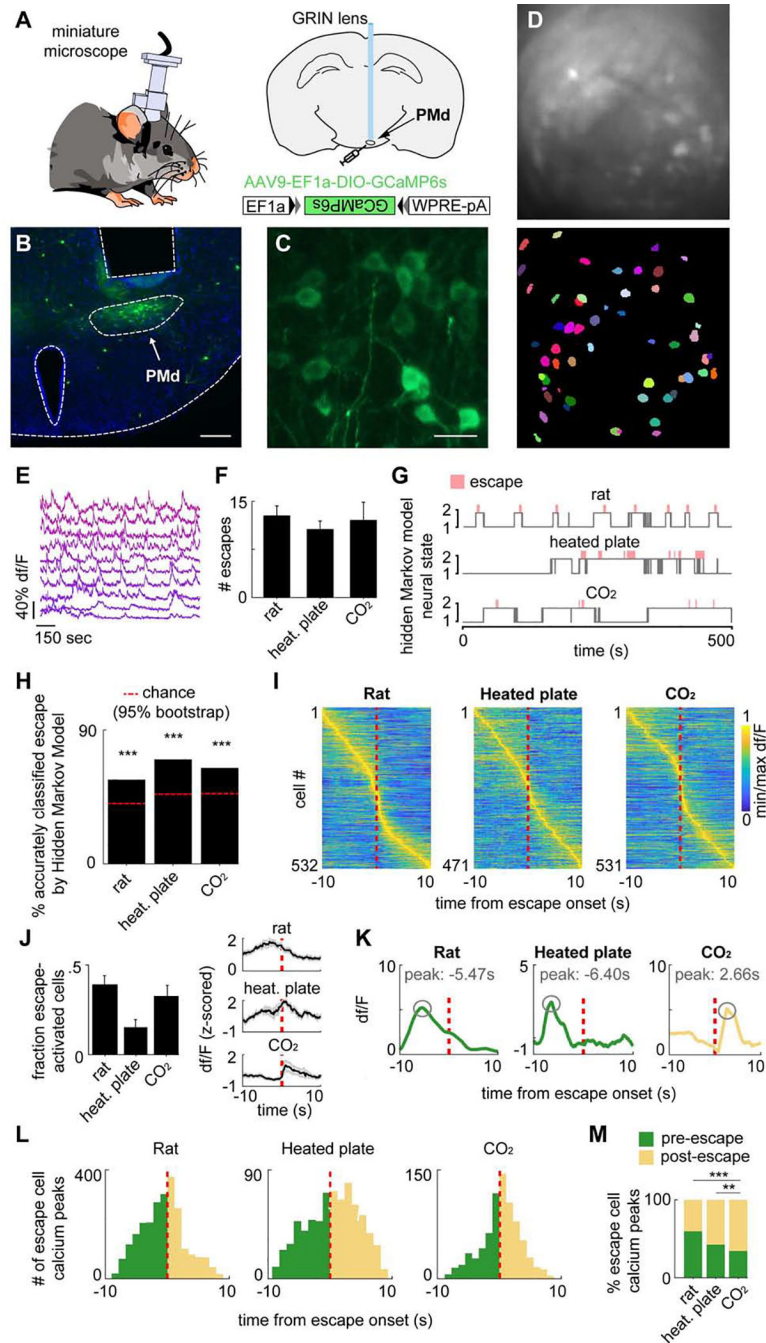
**Figure 3. Microendoscopic recordings of the PMd reveal escape-predicting states and higher activation prior to context-specific escapes.**

(A) Diagram of calcium imaging setup and GRIN lens.

(B) Histology of GRIN lens implantation and GCaMP6s expression in the dorsal premammillary nucleus of the hypothalamus (PMd). (scale bar: 200 μm)

(C) 40x times magnified view of histology in (B). (scale bar: 10 μm)

(D) (top) Maximum projection of the PMd field of view. (bottom) Putative cell contours for the same session.

(E) Extracted calcium activity of example cells in PMd.

(F) Escape count in each assay (rat $n$=10, heated plate $n$=9, $CO_2$ $n$=12).

(G) States were extracted from neural data (unsupervised Hidden Markov model (HMM), 2 states). In these examples, the states (gray) separate escape from non-escape epochs (escape=red bar), even though escape information was not part of the input to the model.

(H) The HMM-defined states significantly predicted escape. (chance level=red line; ***p<.001)

(I) Rows depict the mean normalized escape-aligned activity of a cell during rat (left), heated plate (middle) or $CO_2$ (right) assays. (rat $n$=532; heated plate $n$=471; $CO_2$ $n$=531)

(J) (left) Bars depict the fraction of escape-activated cells identified in each threat assay. (rat $n$=10, heated plate $n$=9, $CO_2$ $n$=12) (right) Example traces of mean escape-activated cell activity (+/−1 SEM) aligned with escape onset. (escape count: rat $n$=12, heated plate $n$=10, $CO_2$ $n$=8)

(K) For each escape behavior of each escape-classified cell, the calcium peak was found and its lag, relative to escape onset, was quantified. Examples show peaks that occurred before (rat/heated plate, green) and after escape ($CO_2$).

(L) Histograms show calcium peak count (shown in (K)) relative to escape onset for threat assays. (green=pre-escape; yellow=post-escape; Rat: pre $n$=1686, post $n$=967; Heated plate: pre $n$=295, post $n$=398; $CO_2$: pre $n$=260, post $n$=498)

(M) Bars depict the percent of calcium peaks (shown in (K)) that occurred pre- (green) or post-(yellow) escape. (Fisher's exact test, **p<.01, ***p<.001) (K-M) Only cells significantly modulated by escape were used.
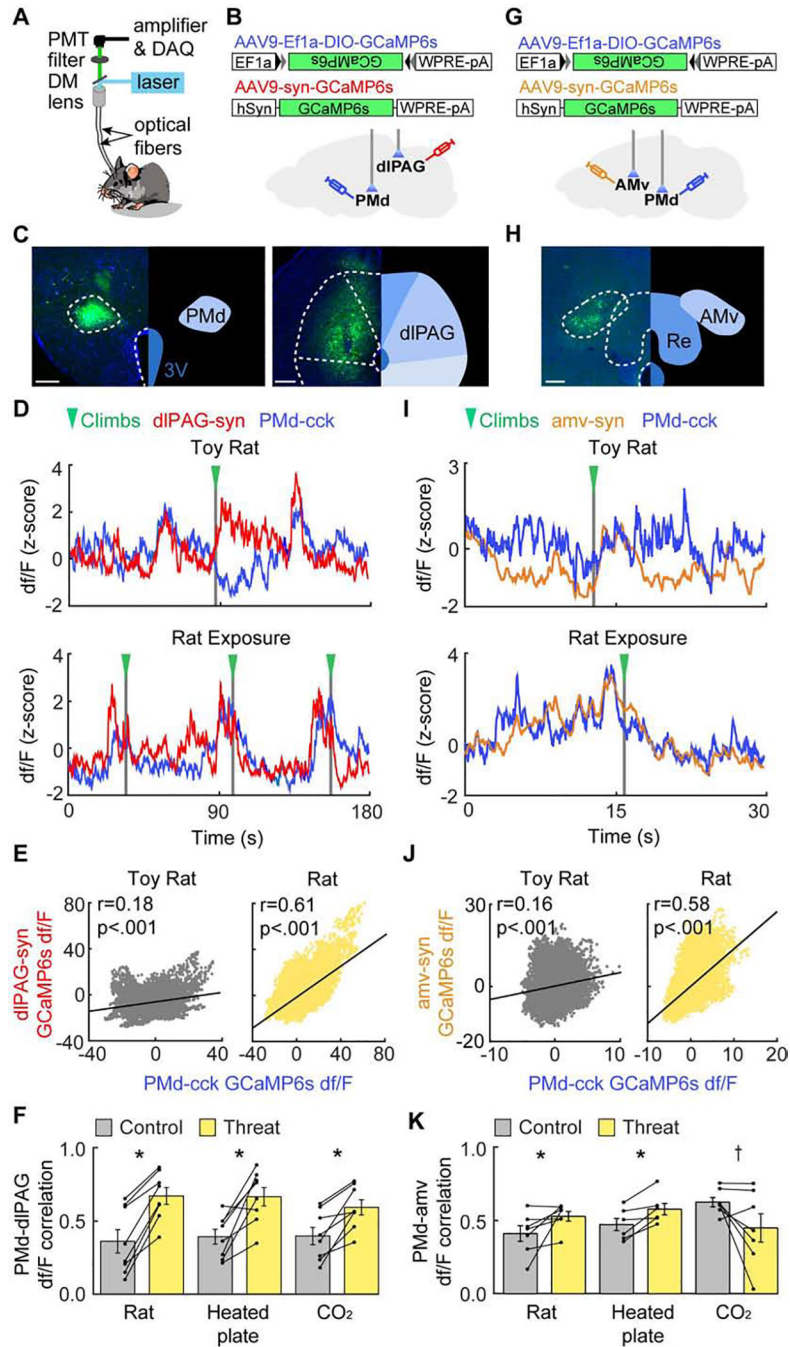
**Figure 4. The PMd-cck→dlPAG-syn circuit becomes more synchronized during threat assays, while the PMd-cck→amv-syn circuit becomes more synchronized only in assays requiring context-specific escape.**

(A) Dual-site fiber photometry setup.

(B) Strategy to express CGaMP6s in PMd-cck cells and dlPAG-synapsin cells.

(C) Histology of GCaMP6s expression in the PMd (left) and the dlPAG. (right; PMd scale bar: 200μm; dlPAG scale bar: 150μm)

(D) PMd-cck and dlPAG traces from toy rat and rat assays.

(E) PMd-cck and dlPAG signals were more correlated during rat than toy rat exposure. (Spearman correlation $r_s$: toy rat: $r_s$=.177, p<0.001; rat: $r_s$=.612, p<0.001)

(F) Average bar plot showing PMd-cck and dlPAG activity were more correlated during threat than control (toy rat, unheated floor and air) exposure. ($n$=8 threat assays, Wilcoxon rank-sum test,*p < 0.05)

(G) Strategy to express CGaMP6s in PMd-cck cells and anterior medial ventral thalamus (amv)-synapsin cells.

(H) Histology of GCaMP6s expression in the amv. (scale bar: 150μm)

(I-K), Same as (D-F), but for mice expressing CGaMP6s in PMd-cck cells and amv-synapsin cells. ($n$=7 for rat, $CO_2$ and controls; $n$=6 for heated plate and control)

(J) Spearman correlation $r_s$: toy rat: $r_s$=.164, p<0.001; rat: $r_s$=.583, p<0.001.
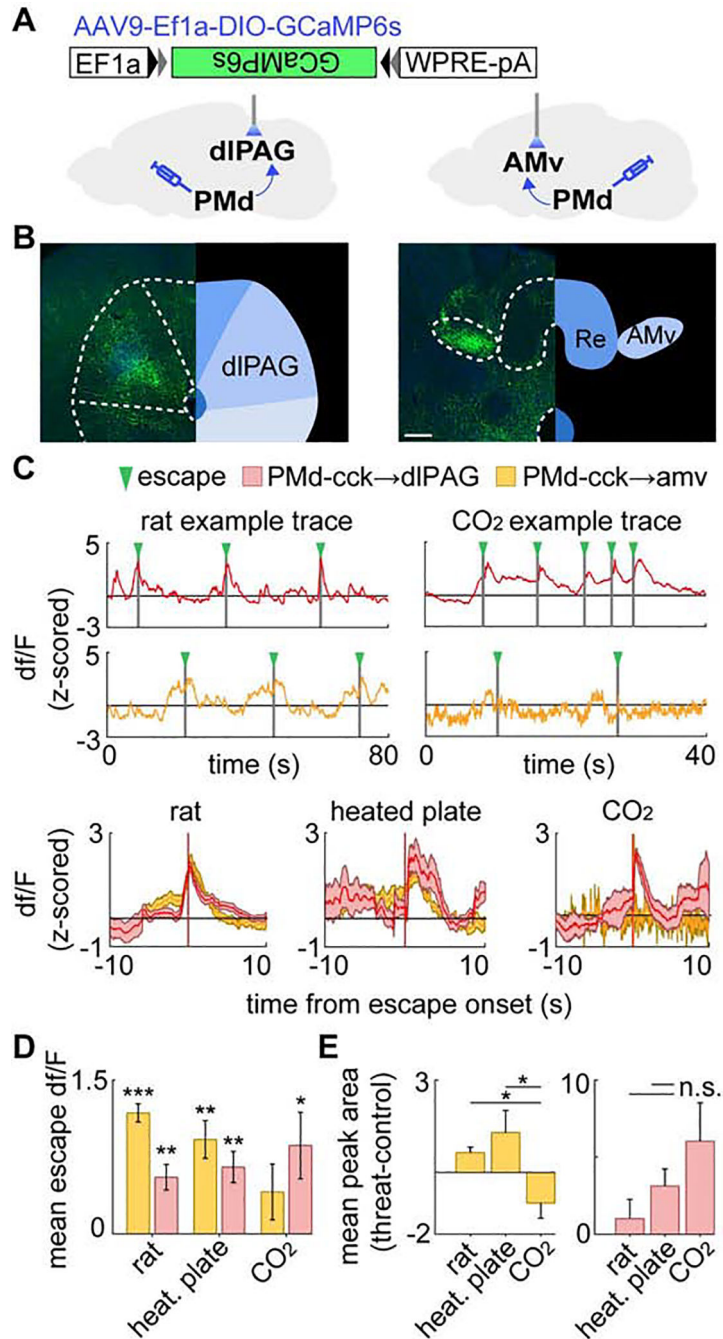
(K) Wilcoxon rank-sum test, *p<0.05, † p=0.078.

**Figure 5. PMd axon terminals in the amv are activated only during context-specific escape while terminals in dlPAG are activated during all escapes.**

(**A**) Recordings were obtained from GCaMP6s-expressing PMd-cck axons terminating in the dlPAG (left) or the amv (right).

(**B**) PMd-cck GCaMP6s-expressing axons in the dlPAG (left) and amv (right). (scale bar: 150 μm)

(**C**) (top) Example fiber photometry traces from PMd-cck axons in the dlPAG (red) and amv (orange) in the rat and $CO_2$ assays. (bottom) Examples of mean escape-triggered activity

from PMd-cck axon terminals in the dlPAG and amv. (escape count, rat: dlPAG n=10, amv n=10; heated plate: dlPAG n=6, amv n=8; $CO_2$: dlPAG n=4, amv n=5)

(**D**) Bars show the mean df/F in a 4s window centered at escape onset for PMd-cck axons in the dlPAG or amv. (n=6 mice)

(**E**) Bars depict the difference of mean positive df/F amplitude. (n=6 mice) \*\*\*p<0.001, \*\*p<0.01, \*p<0.05.
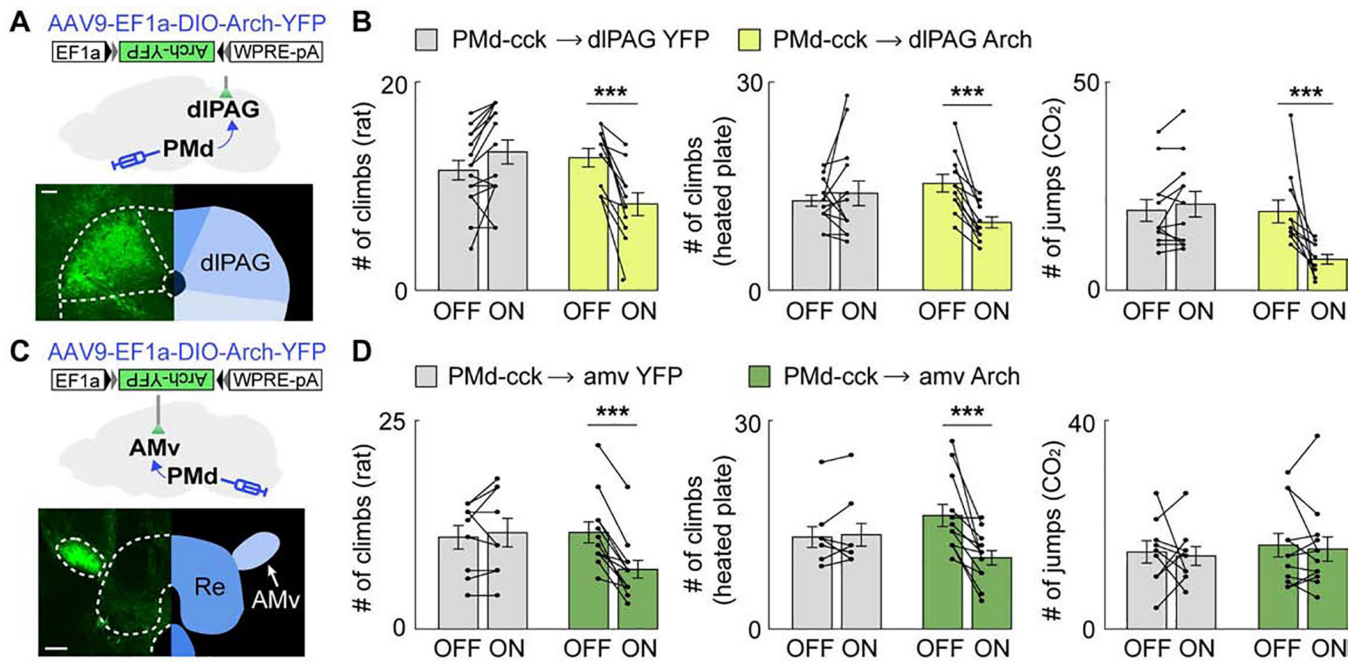
**Figure 6. Inhibition of the PMd-cck→dlPAG projection decreases escape in all threat assays while inhibition of the PMd-cck→amv-syn projection selectively decreases context-specific escape.**

(A) Strategy to optogenetically inhibit arch-expressing PMd-cck axons terminating in the dlPAG (scale bar: 100μm)

(B) Optogenetic inhibition of the PMd-cck→dlPAG projection with green light (532 nm) decreased escape in all assays. (rat: YFP $n$=15, arch $n$=11; heated floor: YFP $n$=12, arch $n$=11; CO$_2$: YFP $n$=14, arch $n$=11, Two-way repeated measures ANOVA followed by Wilcoxon test, ***p < 0.001)

(C) Similar to (A), but with fiber optic cannula implanted over the amv. (scale bar: 150μm)

(D) Optogenetic inhibition of the PMd-cck→amv-syn projection with green light decreased escape count during rat (left), heated floor (middle) but not CO$_2$ (right) exposure. (rat: YFP $n$=9, arch $n$=12; heated floor: YFP $n$=9, arch $n$=12; CO$_2$: YFP $n$=9, arch $n$=12, Two-way repeated measures ANOVA followed by Wilcoxon test, ***p < 0.001) Mean ± SEM.

## KEY RESOURCES TABLE

| REAGENT or RESOURCE | SOURCE | IDENTIFIER |
|---|---|---|
| Antibodies | | |
| Rabbit anti-Fos (Ab-5) | EMD Millipore | Cat# PC38; RRID:AB_2106755 |
| Rabbit anti-NeuN | Novusbio | Cat# NBP1–77686SS; RRRID:AB_11027797 |
| Donkey anti-rabbit IgG-Alexa Fluor 594 | Cellsignal | Cat# 8889; RRID:AB_2716249 |
| | | |
| Bacterial and Virus Strains | | |
| AAV9.hSyn.eYFP.WPRE.bGH | James M. Wilson; unpublished | Addgene # 105539 |
| AAV9.Syn.DIO.EGFP.WPRE.hGH | Ian Wickersham; unpublished | Addgene # 100043 |
| AAV9.hSyn.hChR2.(H134R)-eYFP.WPRE.hGH | (Chan et al., 2017) | Addgene # 26973 |
| AAV9.EF1a.DIO.hChR2(H134R)-eYFP.WPRE.hGH | (Chan et al., 2017) | Addgene # 20298 |
| AAV9-EF1a-DIO-eYFP | (Chan et al., 2017) | Addgene # 27056 |
| AAV9- EF1a-DIO-Arch- eYFP | (Chow et al., 2010) | Addgene # 22222 |
| AAV8.Syn.DIO. mCherry | Bryan Roth; unpublished | Addgene # 50459 |
| pAAV8-hSyn-DIO-hM4D(Gi)-mCherry | (Krashes et al., 2011) | Addgene # 44362 |
| AAV8-Syn-DIO-HM3D(Gq)-mCherry | (Krashes et al., 2011) | Addgene # 44361 |
| AAV9-Syn-DIO-GCaMP6s-WPRE-SV40 | (Chen et al., 2013) | Addgene # 100845 |
| AAV9-Syn-GCaMP6s-WPRE-SV40 | (Chen et al., 2013) | Addgene # 100843 |
| | | |
| Experimental Models: Organisms/Strains | | |
| Cck-IRES-Cre mice | Jackson Laboratories | Stock # 012706; RRID:IMSR_JAX:012706 |
| C57BL/6J mice | Jackson Laboratories | Stock # 000664; RRID:IMSR_JAX:000664 |
| SF1-cre mice | Jackson Laboratories | Stock # 012462; RRID:IMSR_JAX:012462 |
| Software and Algorithms | | |
| MATLAB | Mathworks | https://www.mathworks.com/ |
| ImageJ | NIH | https://imagej.nih.gov/ij/index.html; RRID:SCR_003070 |
| DeepLabCut | Mathis et al., 2018 | http://www.mousemotorlab.org/deeplabcut |
| Miniscope Controller | UCLA Miniscope | https://github.com/daharoni/Miniscope_DAQ_Software |
| Miniscope preprocessing/motion correction | Aharoni et al., 2019 | https://github.com/daharoni/Miniscope_Analysis |
| Extraction of *in vivo* calcium signals | Zhou et al., 2018 | https://github.com/zhoupc/CNMF_E |
| | | |
| Other | | |
| Orca Flash camera | Hamamatsu | https://www.hamamatsu.com/resources/pdf/sys/SCAS0081E_C11440-22CU.pdf |
| Optogenetic Fiberoptic Cannulae | Doric Lenses | MFC_200/240–0.22_MF1.25_FLT |
| Fiber photometry fiberoptic cannulae | Neurophotometrics | FOC_MF_400 |
| Superfrost Plus slides | Fisher Scientific | Cat # 22–037-246 |
| Microendoscope | UCLA Miniscope | http://miniscope.org/index.php/Main_Page |

| REAGENT or RESOURCE | SOURCE | IDENTIFIER |
|---|---|---|
| Nanoinjector | World Precision Instruments | Cat# Nanoliter 2000 |